AD-A016 498

A STRUCTURAL EVALUATION OF RAPID METHODS OF BACKFILLING FOR BOMB DAMAGE REPAIR - PHASE II

John Crawford, et al

Naval Civil Engineering Laboratory

Prepared for:

Air Force Weapons Laboratory

August 1975

AFWL-TR-
74-272

A STRUCTURAL EVALUATION OF RAPID METHODS OF BACKFILLING FOR BOMB DAMAGE REPAIR--PHASE II

John Crawford
James B. Forrest

Civil Engineering Laboratory
Naval Construction Battalion Center
Port Hueneme, CA 93043

August 1975

Final Report for Period April 1973 - August 1974

Approved for public release; distribution unlimited.

AIR FORCE WEAPONS LABORATORY
Air Force Systems Command
Kirtland Air Force Base, NM 87117

UNCLASSIFIED

SECURITY CLASSIFICATION OF THIS PAGE (When Data Entered)

REPORT DOCUMENTATION PAGE

READ INSTRUCTIONS BEFORE COMPLETING FORM

1. REPORT NUMBER: AFWL-TR-74-272	2. GOVT ACCESSION NO.
3. RECIPIENT'S CATALOG NUMBER	
4. TITLE (and Subtitle): A STRUCTURAL EVALUATION OF RAPID METHODS OF BACKFILLING FOR BOMB DAMAGE REPAIR-PHASE II	5. TYPE OF REPORT & PERIOD COVERED: Final Report, April 1973 - August 1974
	6. PERFORMING ORG. REPORT NUMBER
7. AUTHOR(s): John Crawford, James B. Forrest	8. CONTRACT OR GRANT NUMBER(s): MIPR 72-6
9. PERFORMING ORGANIZATION NAME AND ADDRESS: Civil Engineering Laboratories, Naval Construction Battalion Center, Port Hueneme, California 93043	10. PROGRAM ELEMENT, PROJECT, TASK AREA & WORK UNIT NUMBERS: Program Element 63723F, Project 2104 4B04
11. CONTROLLING OFFICE NAME AND ADDRESS: Air Force Weapons Laboratory, Kirtland Air Force Base, NM 87117	12. REPORT DATE: August 1975
	13. NUMBER OF PAGES: 80
14. MONITORING AGENCY NAME & ADDRESS (if different from Controlling Office): Air Force Weapons Laboratory, Kirtland Air Force Base, NM 87117	15. SECURITY CLASS. (of this report): UNCLASSIFIED
	15a. DECLASSIFICATION DOWNGRADING SCHEDULE

16. DISTRIBUTION STATEMENT (of this Report)

Approved for public release; distribution unlimited.

17. DISTRIBUTION STATEMENT (of the abstract entered in Block 20, if different from Report)

Same as block 16.

18. SUPPLEMENTARY NOTES

19. KEY WORDS (Continue on reverse side if necessary and identify by block number)

Civil Engineering
Bomb Damage Repair
Backfill Materials

20. ABSTRACT (Continue on reverse side if necessary and identify by block number)

An analytical model for evaluating the performance of repair systems for bomb-damaged runways is presented. This model consists of a finite element computer code capable of predicting the response of a repaired crater to an applied single wheel load, placed at the center of the repaired surface. Variables investigated during development of the analytical model include different element meshes, number of load steps, material stiffnesses and tension cutoff levels. Background information dealing with application of the model and generation of its input is

(OVER)

DD FORM 1 JAN 73 1473 EDITION OF 1 NOV 65 IS OBSOLETE

UNCLASSIFIED

SECURITY CLASSIFICATION OF THIS PAGE (When Data Entered)

ABSTRACT (Cont'd)

included. Verification of this prediction technique is presented, based upon experimental testing of repaired model craters and repaired prototype 750-pound bomb craters. The prototype crater was repaired using the procedure recommended in Air Force Manual 93-2. The analytical model is shown to give valid predictions of the repair system response as long as reasonable attention is directed toward generation of input information.

CONTENTS

CONTENTS (Continued)

LIST OF ILLUSTRATIONS

Figure

Page

LIST OF TABLES

LIST OF SYMBOLS

$[B]$	Strain/displacement matrix or strain/displacement transformation
$[C]$	Constitutive matrix for plane strain or stress/strain transformation
$\{d\}$	Element displacement vector
E	Young's modulus of elasticity
$\{F\}$	Force vector or global load vector
G	Shear modulus
G_u	Unloading shear modulus
K	Bulk modulus
K_n	Bulk modulus for nth step
K_u	Unloading bulk modulus
$[K]$	Stiffness matrix
$[k_q]$	Quadrilateral element stiffness matrix
P	Potential energy
R, Z, θ	Cylindrical coordinate directions
S, T	Natural coordinates for an element
s, t	Spatial variables in S, T coordinate system
$\{U\}$	Displacement vector
u, v, w	Displacements in the X, Y, Z directions, respectively, or the R, Z, θ directions, respectively
X, Y, Z	Cartesian coordinate directions
z	Spatial variable for Z coordinate direction
γ	Maximum shear strain
ε_G	Volumetric strain caused by gravity
ε_n	Accumulated strain at nth step
ε_V	Volumetric strain
$\{\varepsilon\}$	Strain vector for plane strain
$\{\sigma\}$	Stress vector for plane stress

List of Symbols (Continued)

σ_c	Tension cutoff stress
σ_H	Hydrostatic stress
ν	Poisson's ratio

SECTION I

SUMMARY

This report presents an analytical method for evaluating repair systems for bomb-damaged runways. A computer code is used to predict the response of repaired craters to ''equivalent single wheel'' aircraft loading. Verification for this prediction technique is presented by comparison of computed results and experimental data for a series of crater models constructed and tested at the Civil Engineering Laboratory (CEL). Additionally, a field test of a full-scale repaired crater is discussed.

Numerous approaches have been explored by the Air Force Weapons Laboratory to determine the most effective and efficient method of repairing bomb-damaged runways. These approaches include: an ejecta backfill method using an optimized equipment package; a structural backfill technique employing polyvinyl chloride (PVC) tubing; and a backfill consisting of cellular foam concrete. The latter two methods include the use of a rapid-setting cementitious material known as regulated-set cement.

During an earlier phase of this project (see Reference 1) CEL commenced development of a finite element computer code capable of analyzing the response of a repaired crater to aircraft loading. Experimental studies were carried out both to determine material properties and to provide a basis for evaluation of the applicability of the computer code. Field plate load tests were conducted on model craters that had been repaired using different conventional materials (e.g., pea gravel). An expedient laboratory testing program was used to provide parameter data on the backfill materials for input to the computer analysis. Descriptions of the laboratory investigations, the model field tests, and the basic computer model have been presented in Reference 1. This reference also includes a few preliminary computer code calculations of the response of the repaired model crater.

During the current phase of this project, extensive evaluation of the code was accomplished using the CEL crater tests and, to a lesser extent, the full-scale field tests conducted at Tyndall AFB. The tests, conducted by the Air Force Civil Engineering Center (CEC) at Tyndall Air Force Base in Florida, were

designed to evaluate different repair techniques including the technique outlined in Air Force Manual AFM 93-2 (Reference 2), using AM-2 matting. The results of one of these tests are presented in this report to illustrate the problems associated with prediction and measurement of actual repaired crater response.

The theory and content of the computer code are presented in Sections II and III of this report; the Tyndall tests are described in Section IV; comparisons of code predictions with experimental data are presented in Section V; and conclusions are presented in Section VI.

SECTION II

METHOD OF ANALYSIS

In the finite element analysis of airfield pavements, the continuous pavement system is replaced with a finite number of elements that are related to one another through common points, called nodes (Figure 1). To prescribe the behavior of the finite element system, an approximate displacement field is assumed within each element. For the three-dimensional pavement system shown in Figure 1, approximate displacement modes are required for the X, Y, and Z displacement fields. These modes are expressed in terms of the three translations associated with each of the common nodal points (i.e., u, v, w: the displacements in the direction of the X, Y, Z axes, respectively). In the simplest case, these expressions are linear with the consequence that the edges of an element remain straight after deformation.

The finite element method is based on the theorem of minimum potential energy (see Reference 3 for a detailed treatment of this method). Using the theorem in conjunction with the assumed element displacement functions, relationships between nodal forces and displacements are derived for the element (element stiffness). Assembling the element stiffnesses, the relationship between nodal forces and displacements is obtained for the whole pavement structure (global stiffness) i.e., a set of algebraic equations of the form $[K]\{U\} = \{F\}$ are derived. The unknowns, $\{U\}$, are the displacements (u, v, w) at each node. The constants, $\{F\}$, are the prescribed loads applied to each nodal point. After displacement boundary conditions are prescribed, the set of equations is solved using standard algebraic solution techniques. This yields values of displacement for each nodal point (i.e., $\{U\}$). Combining the displacements at each node with the assumed element displacement expressions, the strain in each element is calculated, and from the strains the stress is obtained. The advantage of the finite element method over the classical methods is that a set of algebraic equations is derived for relating force to displacement instead of a set of partial differential equations. The algebraic equations are readily formed and solved by computer.

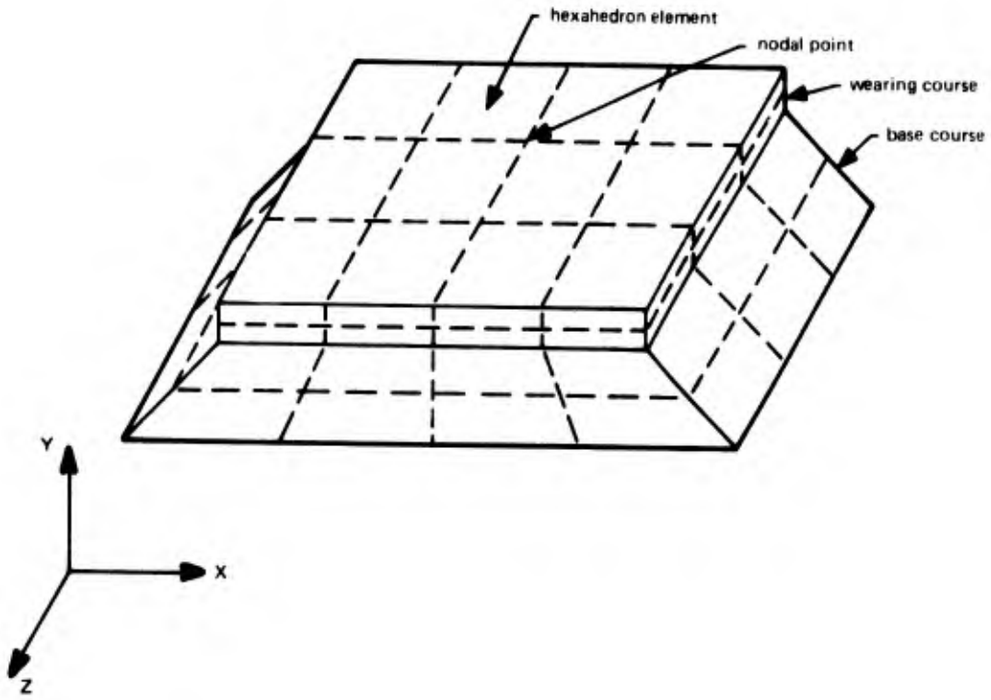

Figure 1. Pavement idealization.

1. SELECTION OF A FINITE ELEMENT ANALYSIS TECHNIQUE

In selecting the type of finite element analysis to be employed, two criteria are used: (1) the degree of idealization necessary to analyze the structure satisfactorily, and (2) the cost of analysis. A pavement system is basically a three-dimensional structure where material properties and loads may be arbitrary and time dependent, and displacements a nonlinear function of the applied loads. The factors determining the cost of running a finite element program are the number of nodes in the structural idealization, the bandwidth of the structural stiffness matrix (defined in Section II.4), the type of element used, and the degree to which the nonlinear and time effects are approximated. To establish an appropriate analysis technique requires balancing the conflicting facets of these two criteria.

For crater repair systems the use of an axisymmetric, piecewise linear, static finite element analysis is deemed an appropriate compromise of the above criteria. The following idealization restrictions are inherent in this selection: (1) all geometry and material definition must be axial symmetric; (2) time-dependent effects are not considered; (3) only moderate material nonlinearity is modeled and is approximated as being piecewise linear; and (4) loads applied to the system must be axisymmetric. Figure 2 depicts an axisymmetric model of a two-layer pavement system; on the right is a cross section of a typical mesh (each element is shaped as an annulus of a ring), and on the left is a cross section showing the pavement geometry and material definition.

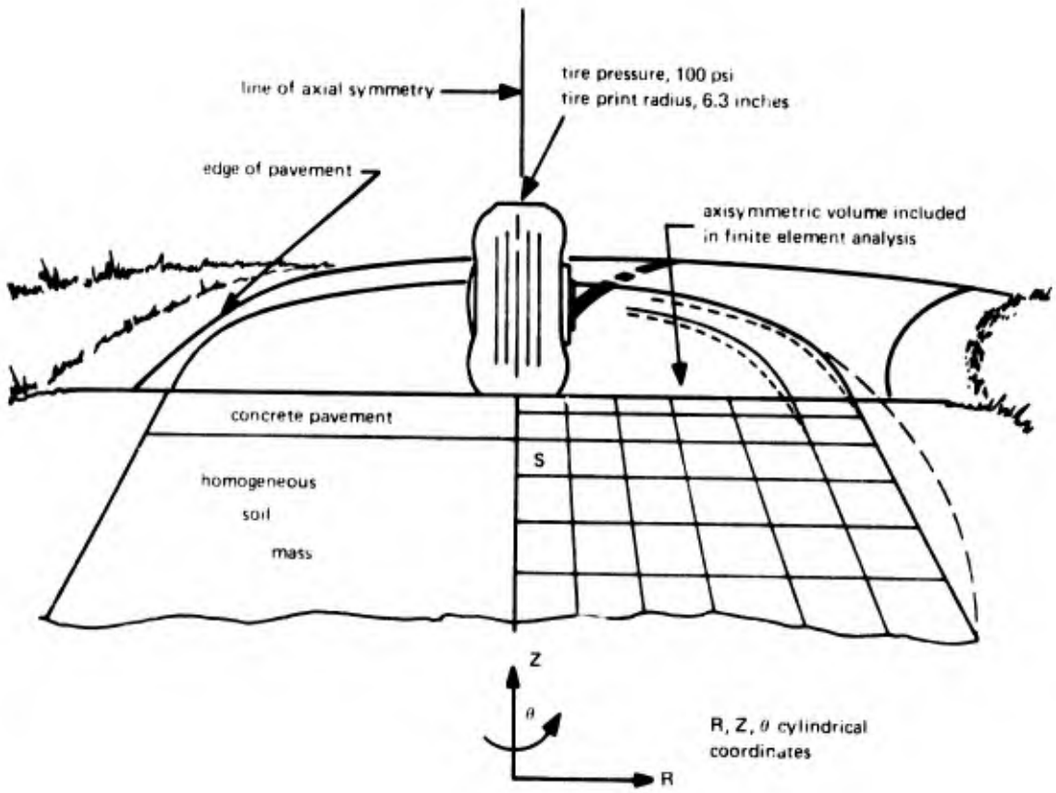

Figure 2. Finite element model of pavement system.

2. THEOREM OF MINIMUM POTENTIAL ENERGY

The theorem of minimum potential energy is used to derive the governing equations for the finite element method and may be written as:

$$\delta P = 0$$

where

$$P = \sum_{i=1}^{I} P_i \tag{1}$$

$$P_i = \frac{1}{2} \int_{\substack{\text{volume} \\ \text{of} \\ \text{element i}}} \{\varepsilon\}^T [C] \{\varepsilon\} \, dV - \int_{\substack{\text{surface} \\ \text{of} \\ \text{element i}}} \{\delta\}^T \{\tau\} \, dS \tag{2}$$

and $\frac{1}{2} \{\varepsilon\}^T [C] \{\varepsilon\}$ = strain energy density

$\{\tau\}$ = prescribed surface tractions

$\{\delta\}$ = surface displacement field

I = number of elements

P_i = potential energy for ith element

3. QUADRILATERAL ELEMENT STIFFNESS

The element used in this report is an axisymmetric quadrilateral (Figure 3). In this section the element stiffness, [k], is developed. To begin the development, an expression for the displacement field must be assumed within each element. The possible deformation patterns of an element as well as the whole structure are governed by this selection. To aid in this selection, the following general criteria can be derived from the governing theorem: (1) the displacement pattern must be continuous within an element and across element boundaries, and (2) the spatial derivatives of displacement must be piecewise continuous. For a more complete discussion of the displacement function selection see Reference 4.

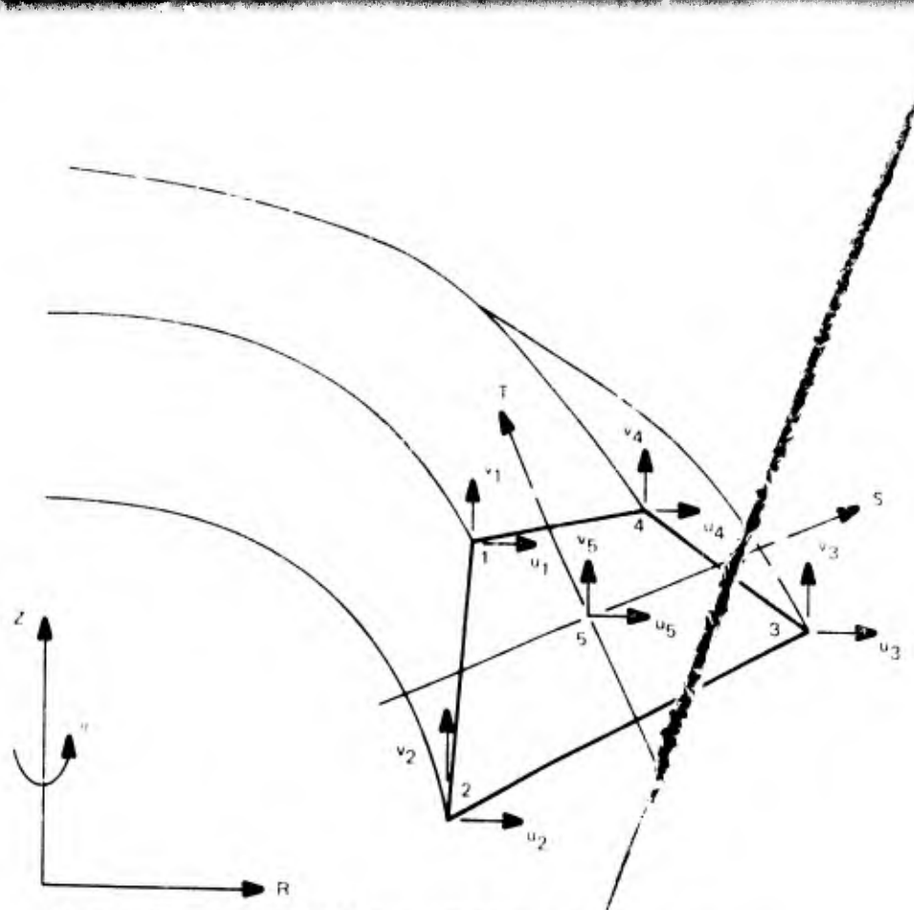

Figure 3. Axisymmetric quadrilateral element.

The general form of the displacement field assumed for this report is:

$$D = \alpha_1 + \alpha_2 s + \alpha_3 t + \alpha_4 s t + \alpha_5(1 - s^2)(1 - t^2) \qquad (3)$$

where α = unknown constants to be solved for

s, t = natural coordinates of the quadrilateral (s and t equal -1 or 1 at the element corners and zero at the centroid)

D = u or v displacement (displacement in the R and Z coordinate directions, respectively; because of axial symmetry, there is no displacement with respect to the θ coordinate)

This displacement field results in a linear variation of displacements along the edges of the quadrilateral; thus, displacement compatibility along element edges is ensured by specifying displacement compatibility only at the nodes. This field satisfies the restrictions imposed by the minimum potential energy theorem (i.e., displacement continuity over the entire body and piecewise continuous derivatives of displacement).

The general form of the element stiffness matrix is:

$$[k] = \int_{\substack{\text{volume} \\ \text{of} \\ \text{element } i}} [B]^T [C] [B] \, dV \tag{4}$$

where $[B]$ = strain/displacement transformation

$[C]$ = stress/strain transformation

That is, $\{\varepsilon\} = [B]\{d\}$, and $\{\sigma\} = [C]\{\varepsilon\}$. The strains, $\{\varepsilon\}$, stresses, $\{\sigma\}$, and displacements, $\{d\}$, considered in this development are:

$$\{\sigma\} = \begin{Bmatrix} \sigma_r \\ \sigma_z \\ \sigma_\theta \\ \sigma_{rz} \end{Bmatrix} \qquad \{\varepsilon\} = \begin{Bmatrix} \varepsilon_r \\ \varepsilon_z \\ \varepsilon_\theta \\ \varepsilon_{rz} \end{Bmatrix} \qquad \{d\} = \begin{Bmatrix} u_1 \\ v_1 \\ u_2 \\ v_2 \\ u_3 \\ v_3 \\ u_4 \\ v_4 \\ u_5 \\ v_5 \end{Bmatrix} \tag{5}$$

The details of the element stiffness development are given in Reference 4.

Associated with each element is a 10 row by 10 column stiffness matrix having 10 degrees of freedom. The displacements associated with node point 5 are expressed in terms of the displacements of points 1 through 4 by matrix partitioning and are eliminated from the system. This produces an 8-degree-of-freedom quadrilateral and an 8 x 8 quadrilateral element stiffness, $[k_q]$.

4. GLOBAL STIFFNESS MATRIX AND LOAD VECTOR

The global stiffness matrix, [K], is the summation of all the element stiffness matrices, $[k_q]$. The stiffness matrix, [K], possesses several properties that are invaluable in computer computations (Figure 4). All coefficients lie in a narrow band along the diagonal and are symmetric about the diagonal.[1] Because of this only the shaded area in Figure 4 need be stored in computer memory. Moreover, the equations are well-behaved, and solutions are obtained without need for matrix conditioning. The solution time is proportional to the number of equations multiplied by bandwidth squared.

Loads are usually applied to the structure by specifying pressures on the surfaces of the elements. The global load vector, {F}, (which represents the

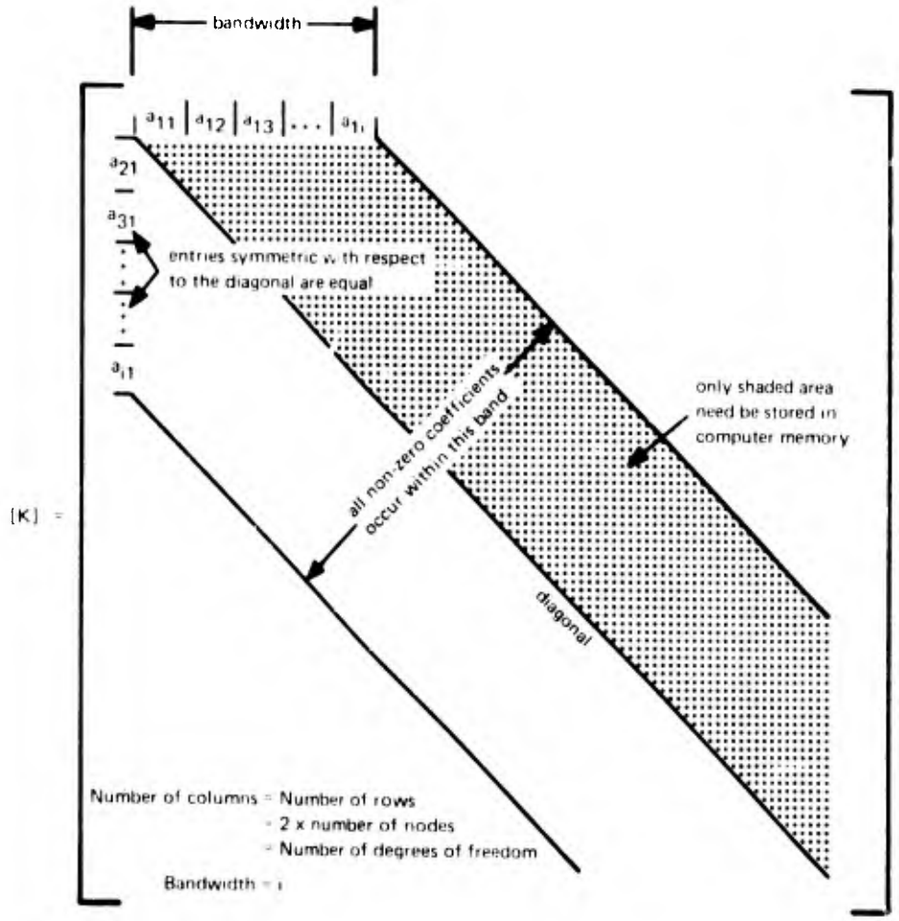

Figure 4. Structural stiffness matrix.

[1] Bandwidth is equal to the maximum difference in node number associated with any one element multiplied by 2, plus 2.

Z-coordinate forces applied at each node since no forces are usually applied along the R-coordinate) is obtained by distributing the force, which results from multiplying the area of the element's surface times the tire pressure, to the nodes at each end of the element's side.

5. BOUNDARY CONDITIONS

Each degree of freedom (i.e., nodal displacement) may be fixed or free. Columns and rows associated with the fixed degree of freedom are removed from the stiffness matrix, [K], and the load vector {F}, and they do not enter into the computational effort.

6. RECOVERY OF RESULTS

The matrix equation for the nodal displacements is:

$$[K]\ \{U\} = \{F\}$$

Gaussian elimination is used to solve these equations, obtaining {U}, i.e., the nodal displacements. The element strains are derived from the nodal displacements of each element (i.e., {d} where u_5 and v_5 are computed from the element's corner displacements contained in {U}) using the strain/displacment matrix, [B]:

$$\{\varepsilon\} = [B]\ \{d\}$$

The strains are computed at the element's centroid (i.e., s = 0, t = 0) and are considered constant over the element. Stress is computed using the constitutive matrix, [C]:

$$\{\sigma\} = [C]\ \{\varepsilon\}$$

Because the strains are constant, the stresses are also constant within an element.

7. ANALYSIS OF NONLINEAR MATERIALS

The analysis of nonlinear materials generally consists of a sequence of ''linear-like'' analyses (referred to as steps), which are related to one another. At each step a linear response of the structure (displacement, stress, and strain) is computed. The material parameters used during a step for each element are determined from the response of the element computed in the previous step. The outcome of such an analysis is a sequence of linear responses. Taken as a whole they represent a nonlinear response to the applied load. (Mathematically, this is known as a linear piecewise approximation of a nonlinear function.)

The particular nonlinear technique used in this report is named the ''initial tangent method''; the model illustrated in Figure 2 will be used to demonstrate the technique. In this example a single wheel is being supported by a concrete surface upon a single layer of soil. To simplify the discussion, only the response of a single soil element will be considered, marked S in the figure. The soil's nonlinear material properites are shown in Figure 5; for simplicity only hydrostatic stress [$\sigma_H = (\sigma_R + \sigma_Z + \sigma_\theta)/3$] versus volumetric strain [$\varepsilon_V = -(\varepsilon_R + \varepsilon_Z + \varepsilon_\theta)$] will be considered, and material unloading and preloading is omitted. Five steps will be used to approximate the nonlinear response.

For each step, the response of the soil element will be computed for 1/5 of the total load (i.e., 20 psi). At the beginning of the nth step, the element's bulk modulus (K_n) is computed based on the strain in element S at the end of the previous step (ε_n). Thus, for the first step, where $\varepsilon_1 = 0$, K_1 is the tangent at the beginning of the material curve. Because of the linear approximation, an error is accumulated at the end of each step such that the material curve the element ''sees'' shadows the curve derived in the laboratory. The degree to which the shadow approximates the measured curve is for this example improved merely by increasing the number of steps used for the nonlinear analysis. The responses computed during each step are cumulatively added to those of the previous steps, resulting at the end of the last step in the response of the pavement to the total applied load (for this example, 100 psi).

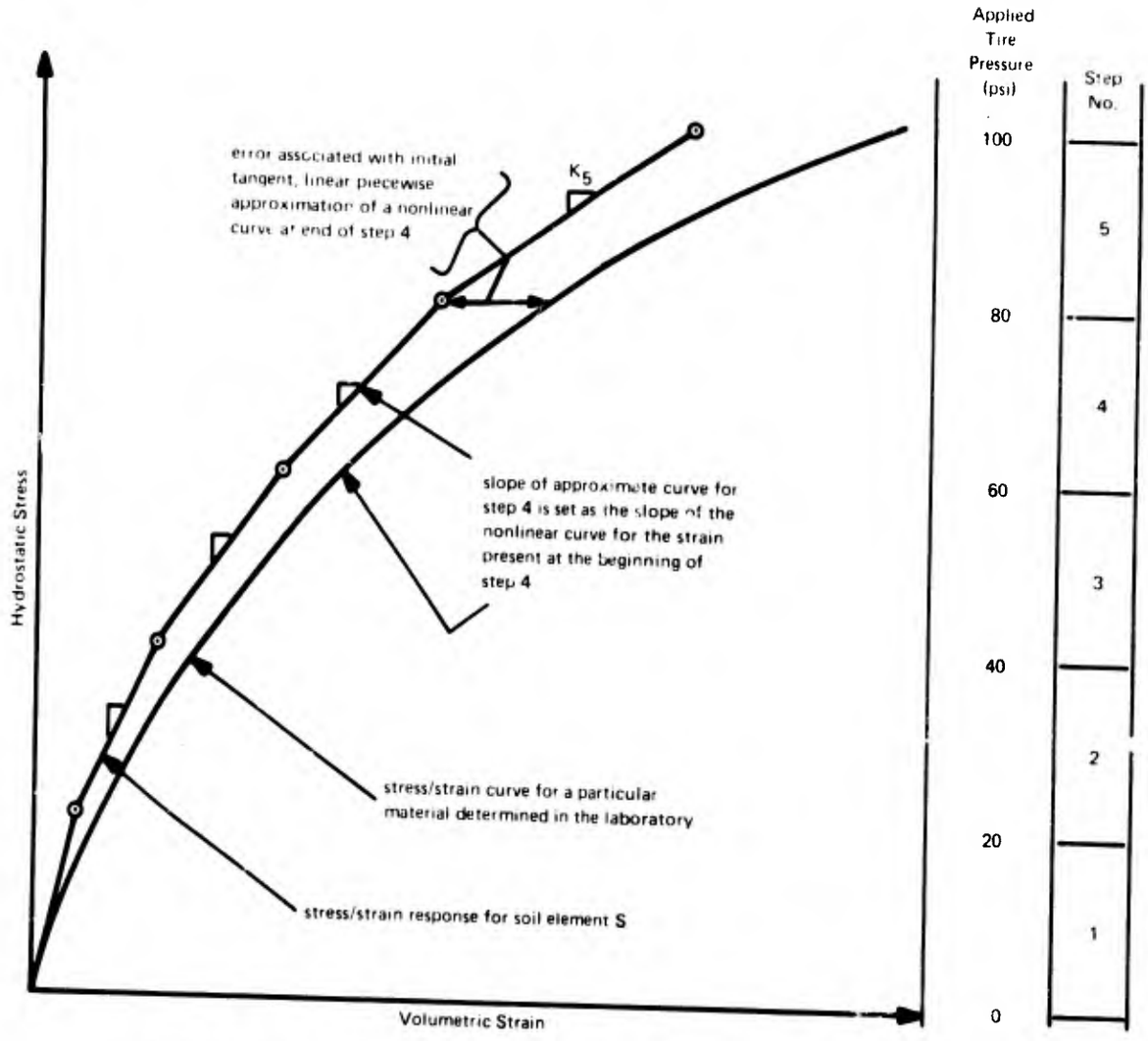

Figure 5. Step-wise approximation of nonlinear behavior.

8. SELECTING A MESH AND NUMBER OF STEPS

Using a quasi-linear displacement field to derive the element stiffness results in the stress/strain field being nearly constant within an element. This result is the primary factor in determining mesh selection: where the gradient of the stress/strain field is large, more elements are needed; conversely, where the stress/strain is relatively constant, fewer elements are needed. The mesh is also affected by geometry and material boundaries.

Figure 6a depicts an axisymmetric finite element model of a repaired bomb crater in an airfield pavement. Small elements are placed directly under the tire where the stress/strain gradient is high. Large elements are used farther

from the load because the stress/strain field is relatively constant. Various odd-shaped elements are used to match the material boundaries. To accommodate the spreading of the load, the outside edge of the mesh is slanted outward. The depth of the mesh is either fixed by a ''hard'' soil layer or at a depth where no significant strain occurs in the soil. This is usually determined by trial and error where element layers are successively added to the bottom of the mesh (thus increasing its depth) until the change in peak displacement between successive runs is less than 10%. Such a process is treated in Section V.1. The width of the mesh is set by a similar process, while the slope of the side is usually taken as 30 degrees, based on results reported in Reference 1. The displacement boundary conditions are generally fixed along the bottom and free along the sides.

The number of steps used for the analysis is a function of the degree of nonlinearity present. Five steps have been found to give reasonable results, while using more than 20 steps provides little added benefit. The procedure for this study was to use five steps for all the preliminary calculations needed to establish the various mesh parameters and to use 20 steps for the final runs. (This reduced the error associated with the linear piecewise approximation of the measured material curve to less than 10%.) For this study, only where concrete overlayed a ''soft'' soil resulting in extensive concrete cracking were there significant differences between the 5- and 20-step analyses.

An additional criterion in mesh selection is ease of data preparation. Figure 6b represents an alternative mesh to that of Figure 6a. To minimize preparation of element and nodal data a regular lattice mesh has been constructed. The material interfaces within the soil mass are only approximately defined by changing the element material numbers at the appropriate places. Justification for this sacrifice of detail lies in the approximate nature of the crater's definition. To match this approximation exactly, as in Figure 6a, is unwarranted.

The above presents a reasonable set of specifications for a pavement model of a repaired crater; however, under unusual circumstances or for other types of models, different specifications may be necessary.

Experience is extremely valuable in designing a competent mesh; there are as yet no references known to the authors that describe mesh preparation procedures. The best procedure for acquiring this experience consists of taking a simple problem (e.g., that shown in Figure 6b) and varying each mesh parameter (e.g., element distribution and number, depth and width of mesh, and number of steps). In some circumstances these variations can produce significant changes

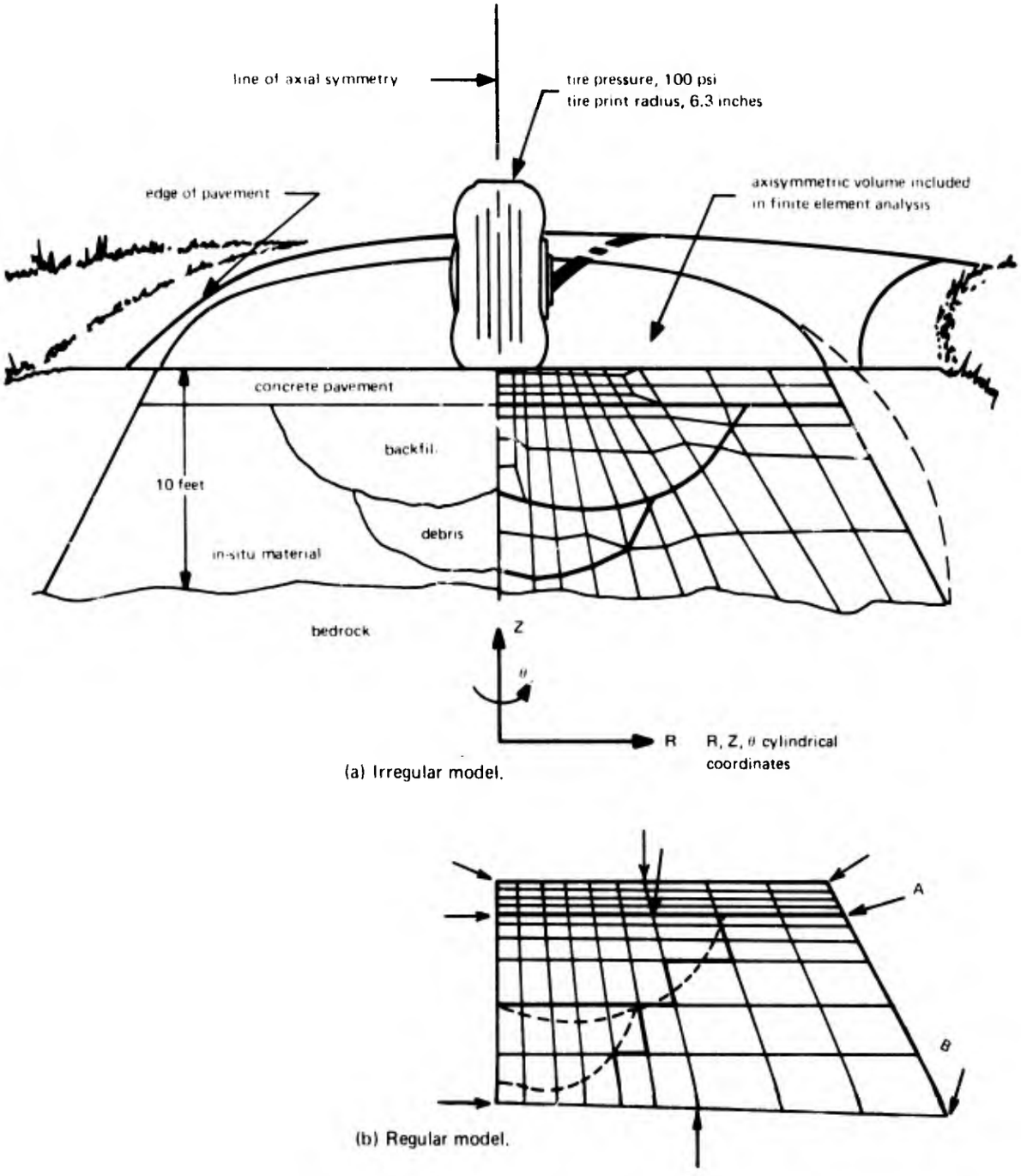

Figure 6. Mesh modeling of repaired crater.

in the responses. It is not possible to insure that the modeling procedures needed for other repaired crater analyses will be the same as those described in this report and care must always be taken, especially on new problems.

SECTION III

PROGRAM FEATURES

1. LAYOUT OF THE COMPUTER PROGRAMS

To perform the finite element analysis, a general purpose linear and nonlinear, static and dynamic axisymmetric code was used (WINDAX, WIlson Nonlinear Dynamic AXisymmetric). The WINDAX code, written in FORTRAN IV, has been used extensively at CEL (see References 5 and 6) for nonlinear dynamic and static analysis. To perform the static nonlinear analysis of the pavement structures, several major improvements to WINDAX were made (e.g., development of the code to permit concrete cracking, changes in the manner in which the nonlinear equations are solved, and addition of gravitational effects). Only those features of WINDAX which apply to static pavement analysis will be described in this report. To use the WINDAX code efficiently, sophisticated techniques must be employed to prepare the input and format the output data. Organization of the human effort and computer pre- and post-processing of finite element data is essential.

To supplement the finite element program, pre- and post-processor programs were written in FORTRAN IV. The pre-processor (GEN2D) program makes possible a simplified generation of the WINDAX input data. The post-processor (PLOT2D) computes and plots response values (e.g., various displacement and stress components) for selected elements and load steps. SCORS (SD 4020) software is used for the plotting.

2. GEN2D PROGRAM

More than half the cost of using WINDAX is incurred during data preparation, i.e., describing the finite element idealization. GEN2D is designed to lessen this burden by at least 90%. Additionally, automated mesh generation encourages experimentation and development of optimal mesh design especially important in nonlinear analysis. GEN2D generates nodal and element data. Nodal data (i.e., the R and Z coordinates and boundary condition associated with each node) are generated using two basic schemes, interpolation and iteration. Nodes may be

generated by interpolation between two known nodes using appropriate input parameters. For example, in Figure 6b, the coordinates of the edge nodes marked A and B were inputed to GEN2D, and the nodes along the edge between them were interpolated using a geometric progression. Additional nodes were interpolated between the nodes indicated by arrows. All other nodal coordinates in Figure 6b were obtained by iteration, where the coordinates of a particular node are obtained by successively averaging the coordinates of nodes connected to it by common element sides. Element data consist of the nodes which lie at the element's corners and the name of material of which the element is made. Elements are generated within or by element layers, where a layer is defined as a row or column of elements that are consecutively numbered and that have a constant nodal difference between consecutive elements. The top row of elements shown in Figure 6b is an element layer, and all the elements within the top four layers (i.e., the concrete material layer) can be generated with a single data card. To generate the mesh shown in Figure 6b, nine nodal cards and three element cards are required.

3. WINDAX PROGRAM

WINDAX is a general purpose axisymmetric solid finite element program for linear and nonlinear, static and dynamic analysis. The code consists of four major sections: data input, element generation, equation solving, and recovery of results; the last three sections are repeated for each load step. WINDAX was written by Wilson and Farhoomand at the University of California at Berkeley (Reference 7). Extensive portions of this code were modified at CEL for this report. WINDAX produces printed output of results and input data for PLOT2D.

Normally most input data for WINDAX is provided by GEN2D with some data input directly on cards (e.g., material definition). After the input is read, a recursive loop for each step of the analysis is initiated. Each element stiffness is generated based on the selected material model and, where applicable, the prior strain and stress state within the element. The element stiffnesses, $\{k_q\}$, are added together to form the global stiffness, [K], and these equations are solved to yield the increment of displacement associated with the step. The incremental stresses/strains are then computed. The incremental responses are added to those of the previous steps to form the nonlinear response of the structure. This process is repeated for each step of the analysis.

4. MATERIAL MODEL

Performing the finite element analysis requires the use of mathematical models that approximate the stress/strain relationships of the pavement materials. Moreover, it is convenient to have a single format to specify the different material models; for WINDAX the bulk modulus, K and shear modulus, G, are used as the primary material parameters. Table 1 lists the material models available in WINDAX.

a. Linear and Nonlinear Models

The linear model used in WINDAX is specified by using K and G. K and G may either be directly derived from experimental data or computed from other material constants such as E (Young's modulus) and ν (Poisson's ratio) by the relationships:

$$K = \frac{E}{3(1 + \nu)}$$

$$G = \frac{E}{2(1 + \nu)}$$

The nonlinear model was adopted from the work described in Reference 8 and is generally applicable to confined noncohesive soil. This model allows the use of

Table 1. Material Models in WINDAX

Material Type	Concrete and Asphalt	Soil
Linear, elastic	K, G	K, G
Elastic with tension cutoff	K, G, σ_c	K, G, σ_c
Linear, nonelastic	not available	K, G, K_u
Nonlinear, elastic	not available	K and G as functions of ϵ_V
Nonlinear and inelastic	not available	K, G, K_u as functions of ϵ_V and σ_c

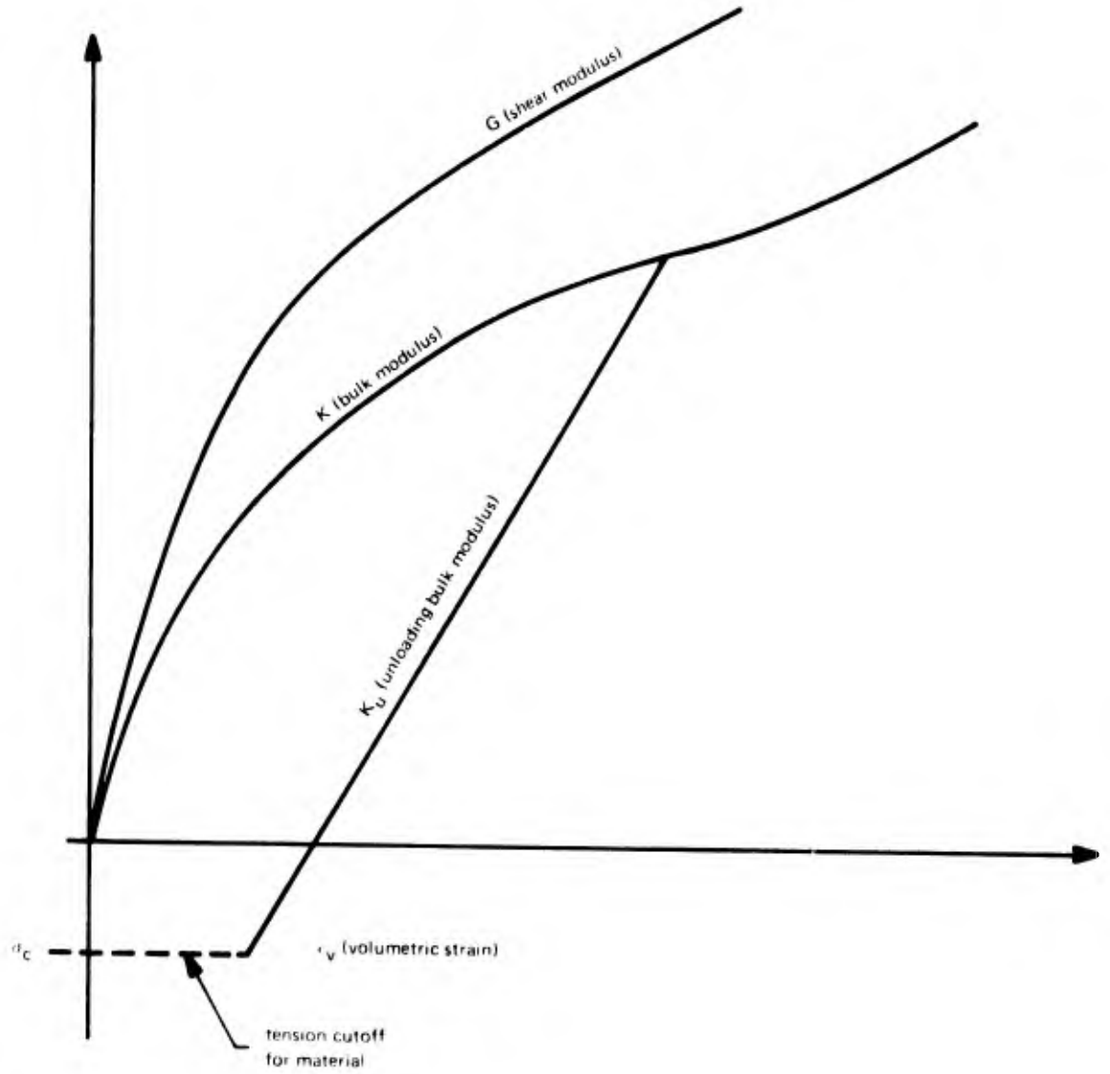

Figure 7. Nonlinear material characterization.

curves that represent material parameters as functions of ε_V [negative volumetric strain, $\varepsilon_V = -(\varepsilon_R + \varepsilon_Z + \varepsilon_\theta)$] to represent the nonlinear behavior of soil.

Figure 7 shows a typical nonlinear characterization for a sandy soil. The abscissa represents ε_V, while the ordinate is K, G, or K_u (bulk modulus during unloading). For any nonlinear material, unloading is linear and occurs whenever ε_V decreases between load steps; during unloading, a material is characterized using K_u and G_u [unloading shear modulus, $G_u = (K_u/K)G$]. For nonlinear material, K and G are used only when $\varepsilon_V > 0$; if $\varepsilon_V < 0$, the material is either unloading or is cracked.

b. Tension Cracking Material

Most paving materials exhibit a marked decrease in load-carrying capacity when subjected to tensile loading as compared to compressive loading. To account for this behavior the WINDAX code computes the principal stresses (i.e., σ_1, σ_2, and σ_3) for each element during each step of the nonlinear analysis. These values are compared to σ_c (tension cutoff stress) specified for each element; when σ_1, σ_2, or σ_3 becomes greater than σ_c, the element stiffness associated with that particular direction is reduced by a factor of 1,000 (in effect simulating a crack). The shear stiffness of an element remains unchanged regardless of tensile cracking.

c. Gravitational Influence on Material

The stresses in the soil mass (computed at each element centroid) caused by gravity are computed as hydrostatic pressures using the expression γz, where γ is the average weight per unit volume of soil, and z is the depth of the element centroid below the surface. The surface is assumed to be at z = 0; thus, values of z for any material below the surface would be negative. When the gravitational influence is included in the analysis, the stiffness for nonlinear materials is based on

$$\varepsilon_V = -(\varepsilon_R + \varepsilon_Z + \varepsilon_\theta + \varepsilon_G)$$

where $\varepsilon_G = \gamma z/K$

SECTION IV

TYNDALL FIELD TESTS

The full-scale crater repair tests, conducted at Tyndall Air Force Base (Reference 9), were primarily designed to assess various repair techniques with respect to speed of repair, equipment requirements, and performance as measured by plate bearing and load cart tests. As part of these tests, three craters were created. Two of these craters (1-1 and 1-2 of Figure 8a) were repaired using the procedures suggested in AFM 93-2 (i.e., filling the crater with ejecta, and capping it with a layer of gravel and AM-2 matting). For crater 1-2, efforts were made to measure strains and displacements during repair and during subsequent plate bearing tests. These data provide useful insights into the problems of analytically predicting crater response as well as pointing out the problems associated with collecting data during such large tests. Only data associated with crater 1-2 are presented in this report.

1. SITE DEFINITION

The site for these tests was located about 10 miles east of the main airfield installations at Tyndall Air Force Base, Florida. The in-situ materials consist of fine, uniform silica sands extending to a few feet above normal ground water elevation. The flat, wooded topography is probably representative of old dune deposits.

The test section for crater 1-2 was constructed by removing the in-situ sand (i.e., Florida sand) down to the approximate depth of the water table and replacing it with an imported material to a thickness of about 10 feet (see Figure 8b). The lower 8 feet of fill was a low plastic sandy clay imported from Alabama, referred to as Eufala clay. The upper 2 feet of fill was a local clayey sand, referred to as Florida clay. Soil index and classification data for both the in-situ sand and the imported fill materials are shown in Table 2. Pavement representative of those existing in NATO countries was constructed using the above material as a subgrade. The pavement section consisted of 12

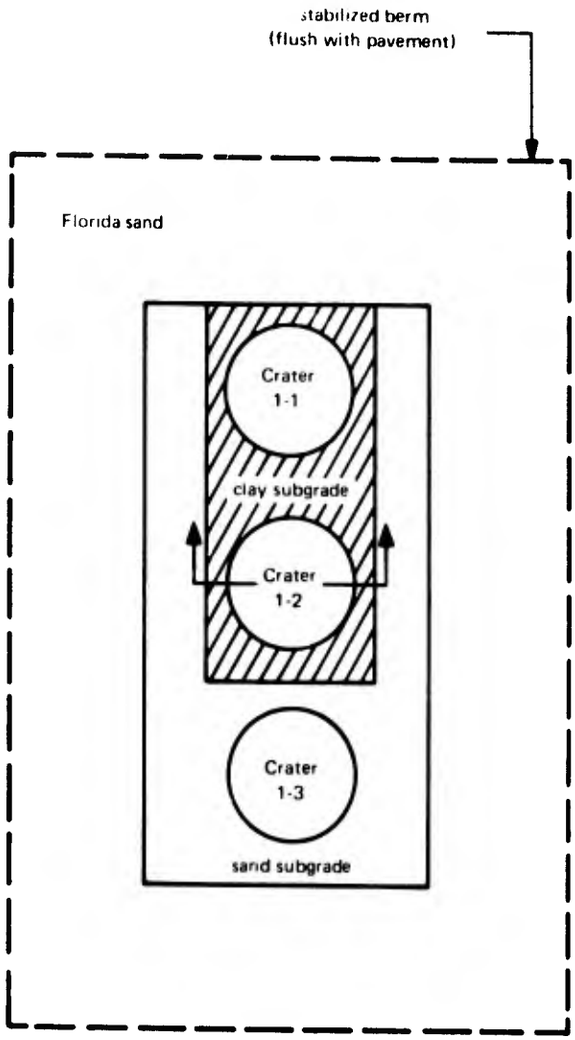

Figure 8a. Plan view of test sections.

inches of graded gravel base course, about 2 inches of uniform sand, 8 inches of portland cement concrete, and two layers of 2-inch-thick asphaltic concrete. The index characteristics of the base materials are shown in Table 2.

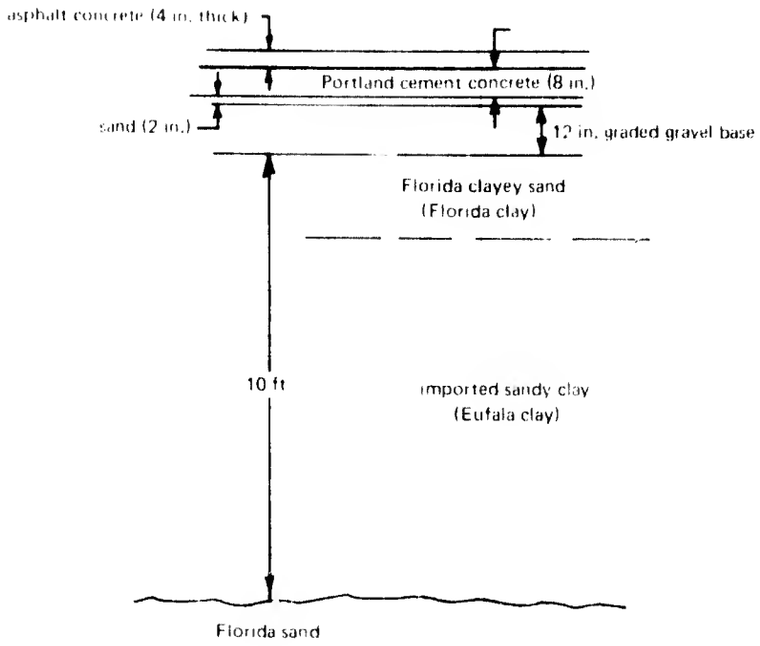

Figure 8b. Test section 1-2.

2. CRATER 1-2

Crater 1-2 was formed by detonation of a 750-pound bomb located 9 feet beneath the asphaltic concrete surface. Following detonation the apparent crater was approximately 11 feet deep (Figures 9 and 10). Excavation at the bottom of the apparent crater uncovered a blackened, compacted layer at a depth of about 12 feet 9 inches, which was assumed to be the lower extent of the true crater. Below the true crater, the reddish sandy clay fill material extended down another 9 inches to the interface with the gray native sand. The apparent crater contained a mixture of red clay lumps and silty sand (Figures 11 and 12). The clay lumps varied in size up to 2 feet on a side. Some blackened platey fragments up to 5 feet in diameter and about 1 foot thick were observed. This material is probably derived from regions immediately adjacent to the bomb, prior to detonation.

Near the center of the apparent crater, the material consisted of a mixture of damp silty sand. This region was below the ground water surface (11 feet below the surface of the pavement). When a hand excavation was made down to the underlying native sand, water commenced to seep into the crater. The loose sandy crater debris appeared to be largely derived from the upper 2 feet of the Florida clay (actually a clayey sand). This material had a shear strength value as indicated by a pocket penetrometer of less than 0.5 ton per square foot

Table 2. Index Properties of Crater Material

Quantity	Florida Sand[a]		Eufala Clay[b]		Florida Clay[c]		Graded Base Course Material[d]	
	Average	Range	Average	Range	Average	Range	Average	Range
In-situ density (lb/cu ft)	86.7	79.6 to 92.7	110.1	84 to 124.6	100	87.2 to 109.7	146.3	143 to 150
Optimum density (lb/cu ft)	97.7	–	120.7	118 to 121	117.4	–	136.3	–
Compaction (% CE 55)	89	–	92	–	85	–	107	–
In-situ moisture (%)	6.0	4.2 to 8.6	16.4	11 to 19.9	13.5	14 to 16.5	2.9	2.3 to 3.4
Optimum moisture (%)	19.1	–	12.5	11 to 14.4	10.3	–	12.1	–
Limits: Liquid (%)	–	–	41	31 to 52	69	–	–	–
Plastic (%)	–	–	18	9 to 28	31	–	–	–
Plasticity index	nonplastic	–	23	–	38	–	–	–
Passing 200 sieve	–	–	47	30.2 to 72.5	23	–	–	–
Unified classification	SP	SP	SC	MH-SC	SC	–	GW	–

[a] Densities determined on final foot of fill.

[b] Approximate thickness of 8 feet.

[c] Limits determined on minus 200 sieve material. High percentage of minus 40 sieve material reduced liquid and plastic limits of this faction to 38 and 19, respectively.

[d] Material contained negligible fines (passing the no. 200 sieve).

(approximately equal to 0.5 kg per sq cm). The large clay lumps indicated shear strengths, as determined by the pocket penetrometer, in excess of 4.5 tons per square foot (see Table 3). This was in excess of the 2 to 2.5 tons per square foot shear strength values indicated for the sandy clay walls of what appeared to be the true crater. This suggests that the clay lumps underwent some degree of compaction during the explosion.

3. REPAIR OF CRATER 1-2

Following a detailed survey of the apparent crater, the sections of uplifted concrete (Figure 13) and thrown out debris were either removed or pushed back into the crater, and backfilling was commenced. Backfilling consisted of placing the debris near the center of the crater with frontend loaders and using a bulldozer to push in material near the edges. The region near the geometric center of the crater was largely hand-backfilled and tamped to facilitate the placement of inductive-type strain gages (see Section IV.4b). The crater was backfilled with debris until it reached within 12 inches of the previous asphaltic surfacing.

Following leveling of the debris, a trailer (see Section IV.4d) was moved into the crater to conduct nondestructive material evaluation tests. During this testing phase, the construction equipment personnel began to place a graded gravel base material around the edges of the crater. Following completion of the nondestructive testing, the placement of the base material was completed (Figure 14). During this phase of the repair procedure, the equipment was used to vigorously pound and compact the surface of the repaired crater, causing large deformations to be recorded by the in-place strain gages. As an example of this, one blow of the dozer blade directly over the crater axis caused a vertical strain of approximately 3% in the upper 12 inches of backfilled debris immediately under the gravel base.

Upon reaching the former grade, the base material was subjected to compaction by a vibratory roller and was roughly leveled by a bulldozer blade. Following testing with the nondestructive test trailer, final grading was carried out with a grader. The backfilled crater was then covered with a preassembled mat made of aluminum AM-2 matting. AM-2 matting is a structural matting made up of extruded aluminum sections 2 x 12 feet x 1-1/2 inches thick.

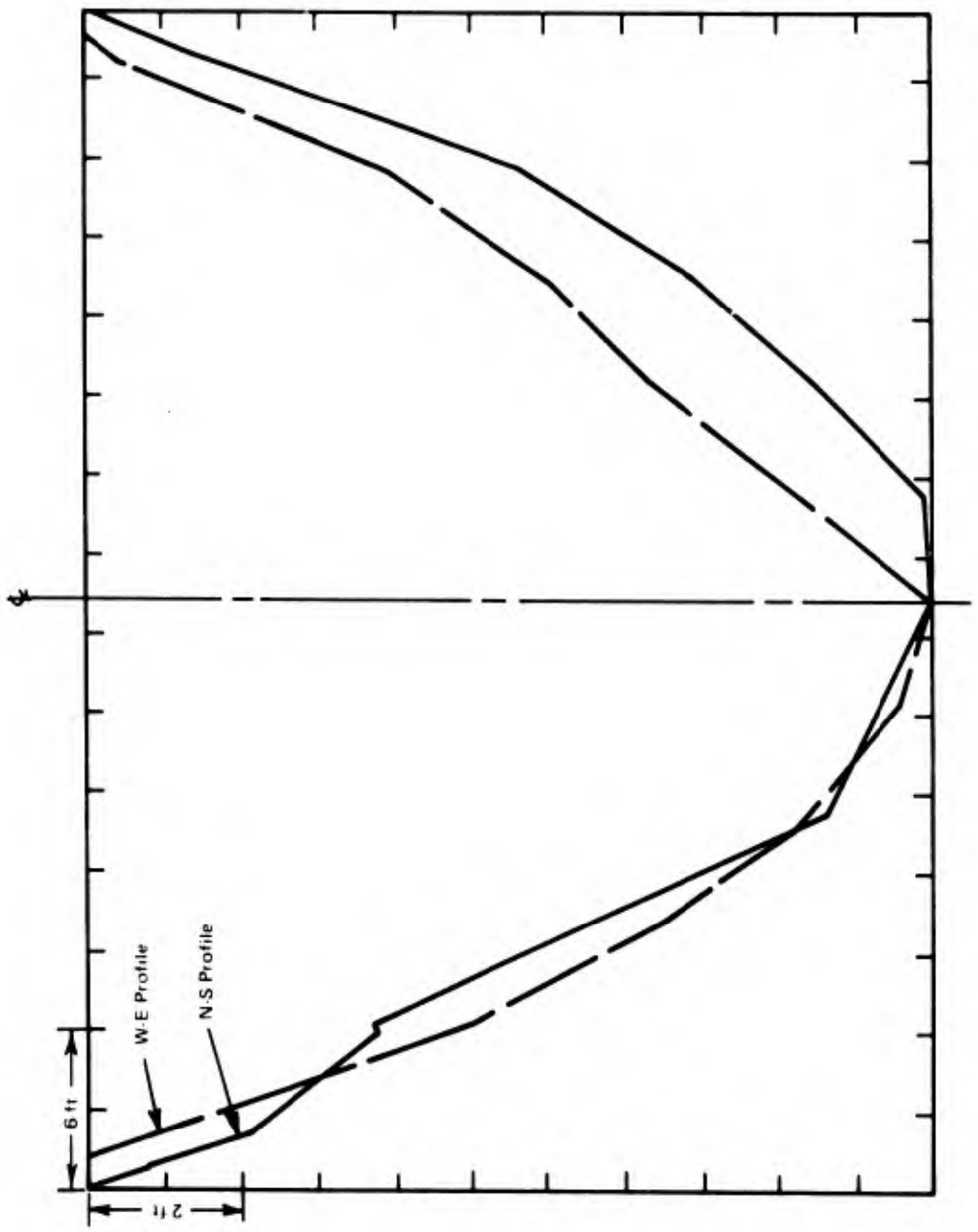

Figure 9. Crater 1-2 profiles.

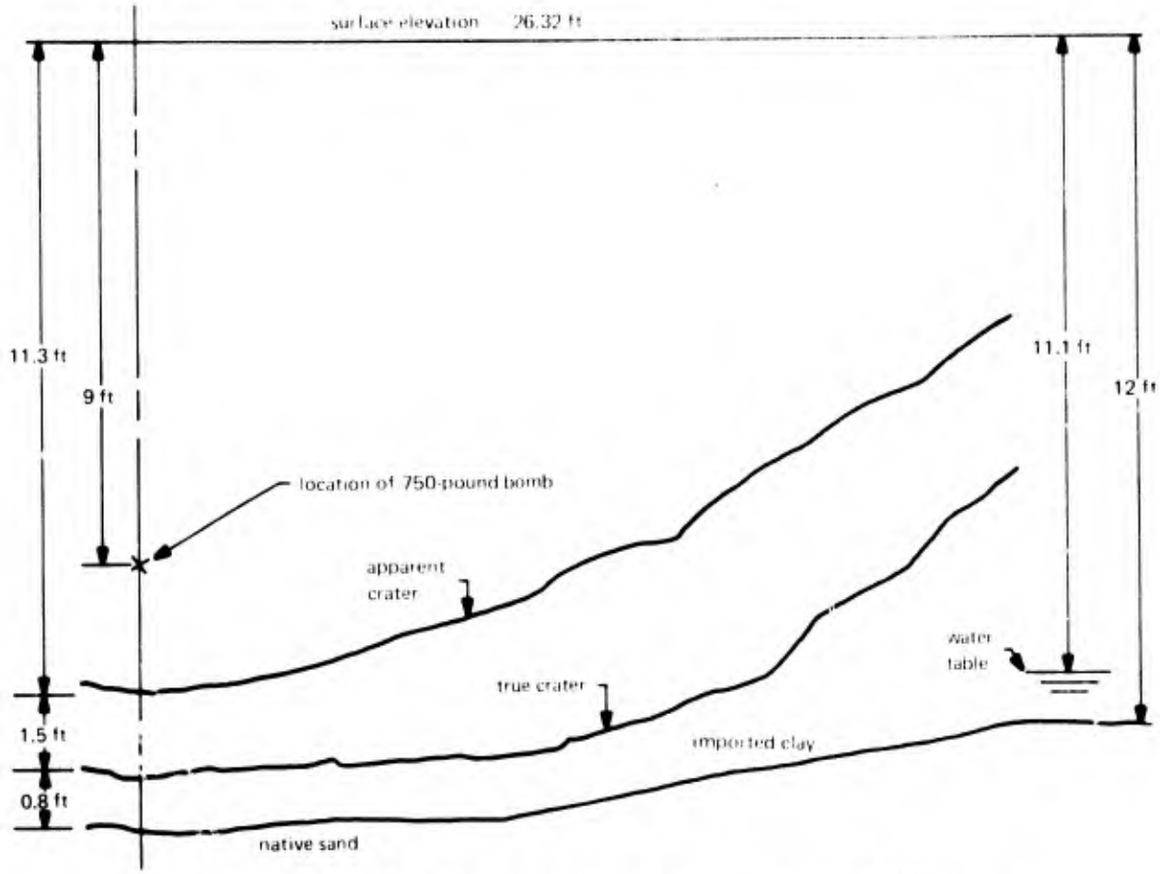

Figure 10. Test section through crater 1-2.

Figure 11. Photo of crater 1-2.

Figure 12. Close-up of crater 1-2 debris.

Table 3. Material Data for Crater 1-2

Material Description	Location	Pocket Penetrometer (lb/sq in.)	Moisture (%)	Dry Density (lb/cu ft)
Native sand	bottom of true crater	–	14.0	100
Sandy (red) clay	apparent crater bottom	7-8	14.0 13.5 14.5	88.4 50.8 102.8
Sandy clay	crater wall	28-35	14.4	87.7
Backfilled debris	9 to 12-foot depth	–	12.4	108.8
Sandy backfilled debris	6 to 8-foot depth	–	6.5	106.9
Sandy backfilled debris	5 feet	–	6.9 9.2	
Compacted rubble	1 to 2-foot depth	–	8.8 8.1	139.5 139.6
Base course material	under AM-2 matting	–	5.4	132.8

Figure 13. Uplifted concrete slabs, crater 1-2.

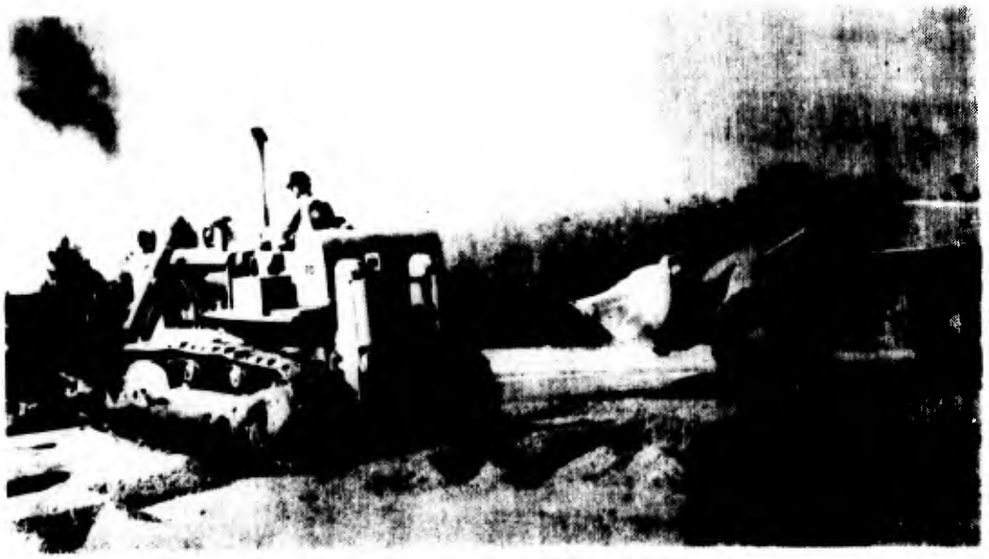

Figure 14. Construction equipment placing base material.

At this stage, load testing of the repaired crater was to have been carried out. Unfortunately, rain precluded this, and further work on the repaired crater was delayed for 3 days. During this 3-day period, surface settlements at the center of the crater were about 7 inches. This required removing the AM-2 matting, rebuilding the gravel base material up to grade, and replacing the AM-2 matting. This resulted in a final thickness of base course material of about 22 inches in the center of the repaired area. Following this, the repaired crater was load tested.

4. INSTRUMENTATION AND DATA COLLECTION

a. Soil Testing

Following the creation of crater 1-2, specimens of the debris were tested in the soils laboratory. It was originally planned that material load response data (later to be used to run the analytical model) be derived from specimens taken from the test site, both before and after cratering. However, this proved to be outside the scope of the project. Nevertheless, specimens have been secured and stored for possible material response determination at a later time. Soil information that was obtained was limited to moisture content and in-situ density determinations following crater formation and during backfilling procedures. Also, a few pocket penetrometer readings were taken, and the appearance of the crater debris was noted. Data obtained on crater 1-2 were shown in Table 3.

Plate-load tests were conducted on both the compacted subgrade and the compacted base material. The results of these load tests, using a 30-inch-diameter plate, are shown in Figure 15. The plate-load tests indicate the subgrade-base combination to be stiffer than the debris subgrade alone, as would be expected. The subgrade modulus measured on the compacted base is about 135 psi per inch (pounds per cubic inch) which is about two-thirds of that expected for a high-quality crushed stone.

Following completion of the final load testing, the AM-2 matting was removed, and field density and moisture tests were conducted on the repaired crater. The results of these index tests are shown in Table 4.

Table 4. Index Tests on Repaired Crater 1-2

Material Description	Thickness (in.)	Dry Density (lb/cu ft)	Moisture (%)	California Bearing Ratio
Base course material	13 to 22	152	5.3	31
Debris subgrade	168	98	4.5	13
Native sand	–	100	15	–

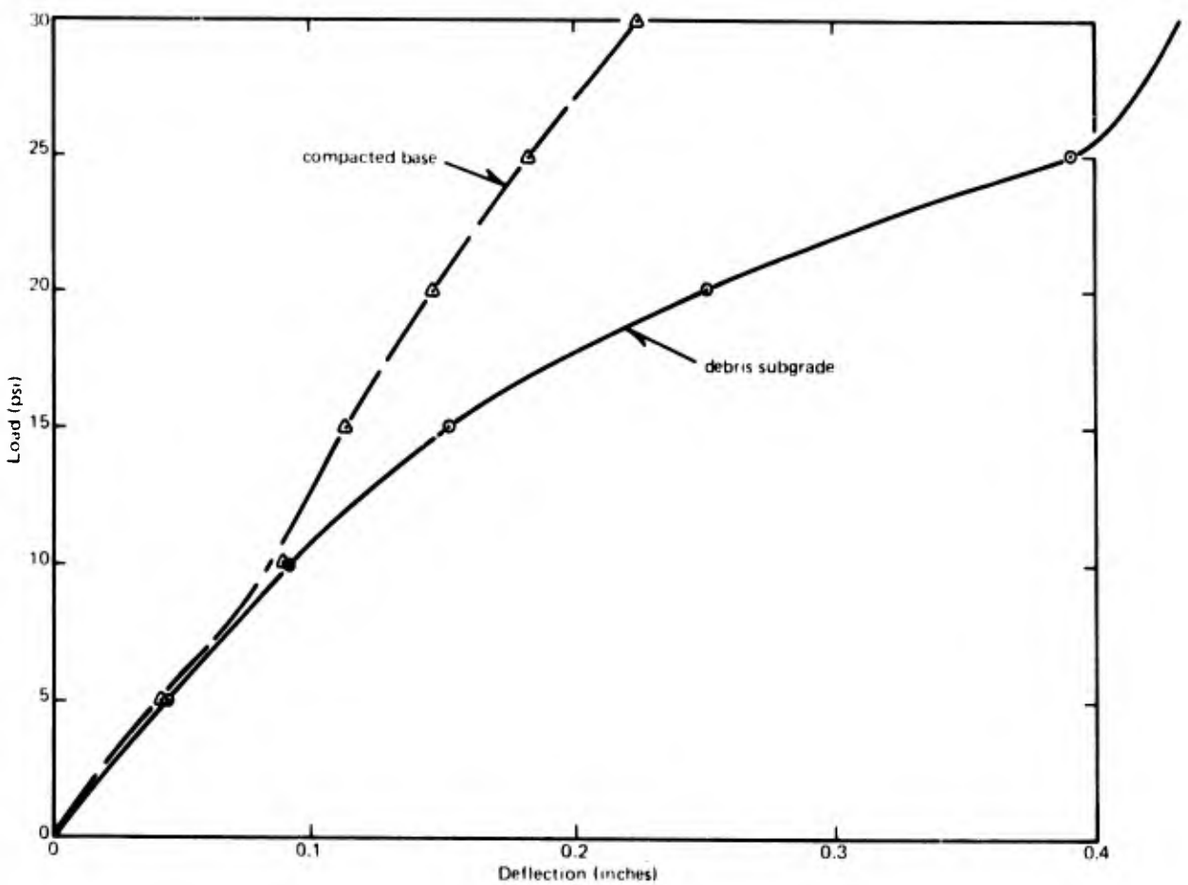

Figure 15. Load-deflection response for 30-inch-diameter plate, crater 1-2.

b. Electroinductance Strain Gages

To evaluate the effectiveness of the repaired crater for supporting aircraft traffic and to provide data for comparison with the analytical model, the deformations occurring in the crater under applied load were measured. Although surface deflections provide the major criteria for evaluating the overall performance of a repair job, surface deflections alone are not capable of indicating how the various regions of the repaired section are deforming.

In order to determine the magnitude of deformation [or strain] occurring at various depths below the loaded surface, strain gages were installed of the inductance type (Reference 11). They are made up of inductance coils embedded in 1/2-inch-thick x 6-inch-diameter epoxy-covered phenolic disks. By exciting one coil and recording the current induced in the neighboring coil, the distance between the coils is measured. These disks were stacked vertically at nominal 6-inch or 12-inch spacings along the centerline of the crater during the backfilling process. In this way vertical strains were recorded throughout the depth of the repaired crater. The disks were placed using precise leveling techniques. At the time of placement, a reading of the gage spacing (or initial gage length) was also taken electronically. Thereafter the disk spacings were monitored electronically, both during the remainder of the crater backfilling process and under applied loads.

Prior to commencement of crater backfilling operations, an inductance coil was placed at the bottom of the crater at the interface between the native sand and the imported fill material. Three more inductance coils were hand-placed at consecutive spacings of 12, 12, and 6 inches. Following this, a cylinder (Figure 16) was placed over the upper inductance coil, and backfilling with the frontend loaders was commenced. At various intervals, the backfilling operation was interrupted, the cylinder raised, and additional inductance coils placed and hand-tamped into position. About four gages were placed during each interruption of the backfilling sequence.

The spacings between all in-place coils were noted electronically at intervals during the backfilling and the compaction processes. This electronic monitoring of displacement commenced from the time each gage or group of gages was installed. In this way a complete record of the vertical deformations occurring during the backfilling and compaction processes was obtained. A summary of these vertical strains after installation but before the load test is shown in Figure 17. This figure also indicates the sequence of filling operations.

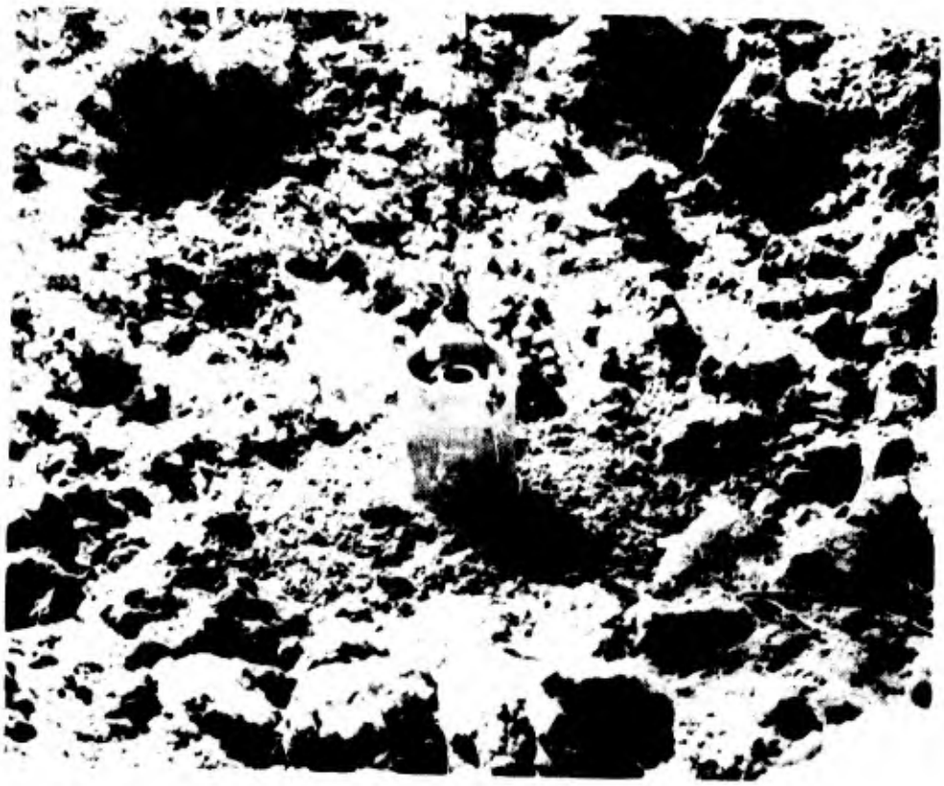

Figure 16. Cylinder used in placement of inductance gages.

Although the inductance coils were initially placed at prescribed depths by means of precise leveling, they began to change their locations immediately following commencement of backfilling operation. For this reason the depth with respect to the surface of each pair of coils was continuously changing.

Since the major purpose of the strain readings during the construction was to show relative trends, absolute depths are ignored, and the measured vertical strains are plotted versus nominal depths in Figure 17. The strain response denoted in Figure 17 from placement of the gages to base completion is noted to increase with depth. The reason for this trend is that the lower inductance coils were placed earlier and have the additional deflections contributed during placement of the upper layers. This figure illustrates the large degree of inhomogeneity of material occurring within the craters.

The strain response indicated in Figure 17, occurring prior to the load tests, is primarily due to long-term settlements and to settlements occurring under random operations at the crater surface, such as leveling, recompaction, placement of the AM-2 matting, etc. The strains associated with long-term

settlements have a distribution that is somewhat similar to the strains occurring during the crater backfilling process. This illustrates two major points: (1) the weaker regions, which contribute larger deformations during the backfilling procedure, also contribute the largest long-term displacements; and (2) long-term displacements occurring following completion of the crater repair are several times larger than those occurring during compaction.

The inductance coil strain readings also contribute another valuable piece of information regarding the behavior of the repaired crater. Following placement of an inductance coil at a nominal depth by means of a precise level, the next lower gage, as recorded electronically, was noted to be beyond the designed spacing. This indicated that the lower gages were settling during the backfilling operation. Since this trend was quite notable during placement of the lower gages, the native sand underneath the crater backfill was undergoing settlement.

During the period immediately following placement of the AM-2 matting and prior to load testing, the repaired crater surface was noted to have settled about 7 inches. Integration of the strains occurring during this period, as shown in Figure 17, would indicate settlements of a similar magnitude. This provides some basis for confidence in accepting the strain gage readings.

c. Plate-Load Tests

Plate-load tests were used to evaluate the effectiveness of the repair technique and to provide for numerical correlations with the computer code. In addition to the 30-inch-diameter plate-load tests conducted during the crater repair operations for use in predicting material response parameters (see Section IV.4a), 12-inch-diameter plate-load tests were conducted upon completion of the repairs. The 12-inch plate roughly approximates the contact area of an F-4 aircraft tire print. The load transmitted through an F-4 tire is approximately 29,000 pounds; however, the plate was loaded up to 50,000 pounds to approximate, in addition, the gross tire load of an F-111. These tests produced load-deflection response; deflection basin profiles, as measured along two mutually perpendicular diameters; and vertical strains, monitored beneath the centerline of the plate.

The load testing was conducted by placing concrete blocks (weighing approximately 4,000 pounds each) on the rear of a low-boy semi-trailer (Figure 18) which had been appropriately placed on the repaired crater. The lip of the

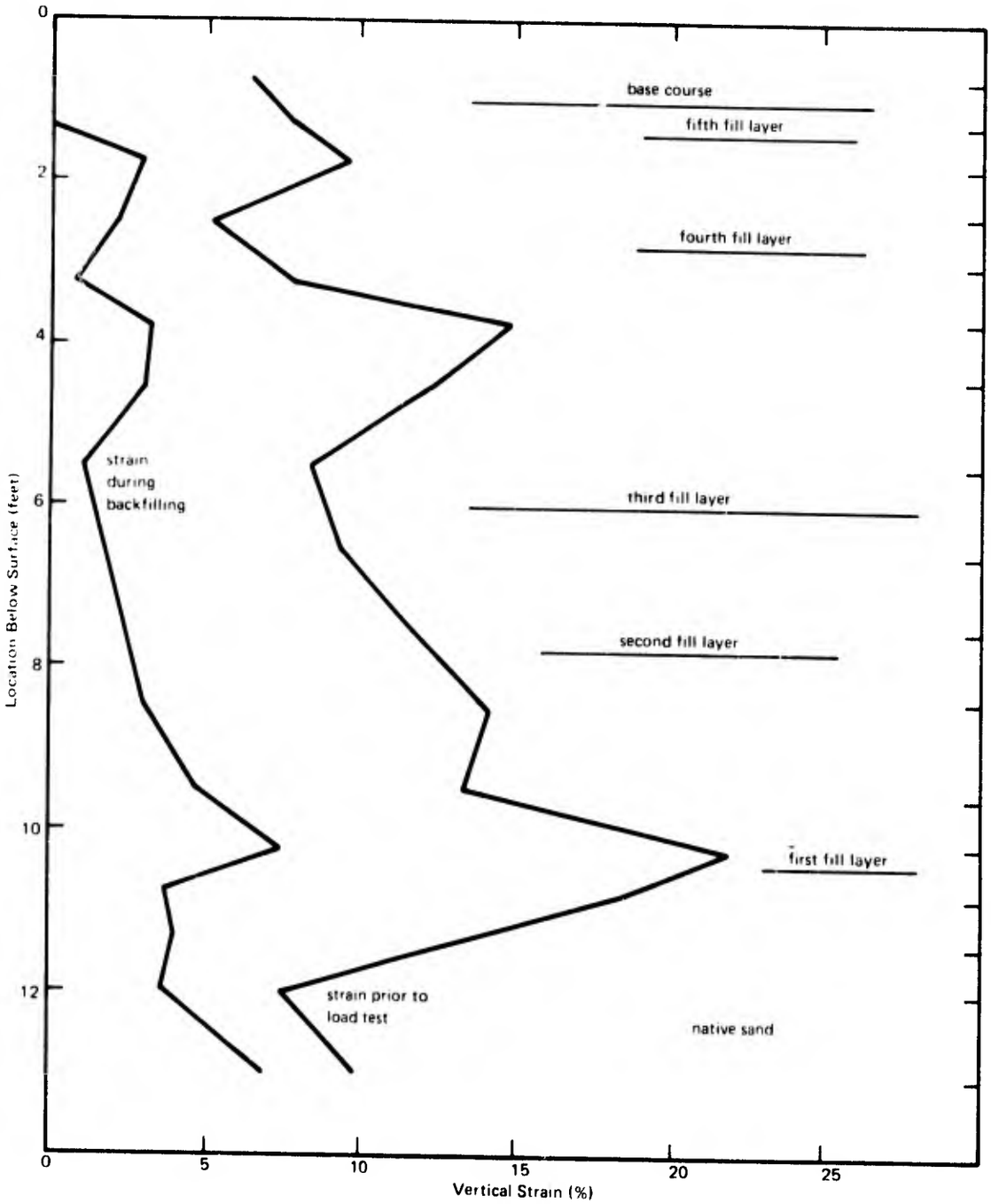

Figure 17. Vertical strains from inductance gages.

beaver-tail was then jacked against to provide a reaction for the desired loading. Results of the plate deflections under load are shown in Figure 19; the curve shows a rather peculiar reverse curvature, indicating a very stiff response at a deflection of about 0.42 inch.

Deflection basin profiles for the AM-2 matting in the vicinity of the plate were extremely erratic and are not reported. During plate loading, the AM-2 mat in the region of the plate rotated along joint lines and appeared to separate from the surface of the underlying base course material.

Vertical strain readings recorded during the plate-load test are shown in Figure 20; strain profiles beneath the center of the loaded plate under various levels of applied load are shown. The data in Figure 20 provide further evidence of the irregularity of the backfill material. Vertical strains are relatively low, particularly over the first few feet of depth beneath the loaded plate. This is largely due to the vigorous compaction achieved immediately prior to placing of the initial base material, when heavy earthmoving equipment was able to gain access to the crater. This degree of compaction was increased during placement of both the initial layer of base material and a subsequent layer (approximately 10-1/2 inches thick at the center).

At depths of 4 to 7 feet, vertical deflections show a tendency to increase; this suggests a region of relatively poorly compacted material. Below this region the vertical strains decrease again. This may be influenced by the degree of compaction at the depths or by the difference in the backfill materials; however, it is primarily due to the lower vertical stresses induced in this region by the applied load.

An integration of the vertical strains occurring in Figure 20 over the upper 12 feet of repaired crater profile suggests deflections on the order of those recorded in Figure 19.

d. Nondestructive Testing

Because of the limited material response data available for operation of the analytical model, it was attempted to utilize nondestructive testing (NDT) techniques for determining the in-situ characteristics of the original and repaired materials. The NDT equipment used is outlined in detail in Reference 10. Very briefly, this equipment consisted of a large trailer van with dynamic loading capabilities and electronic recording equipment (Figure 21). This equipment could perform two types of nondestructive testing.

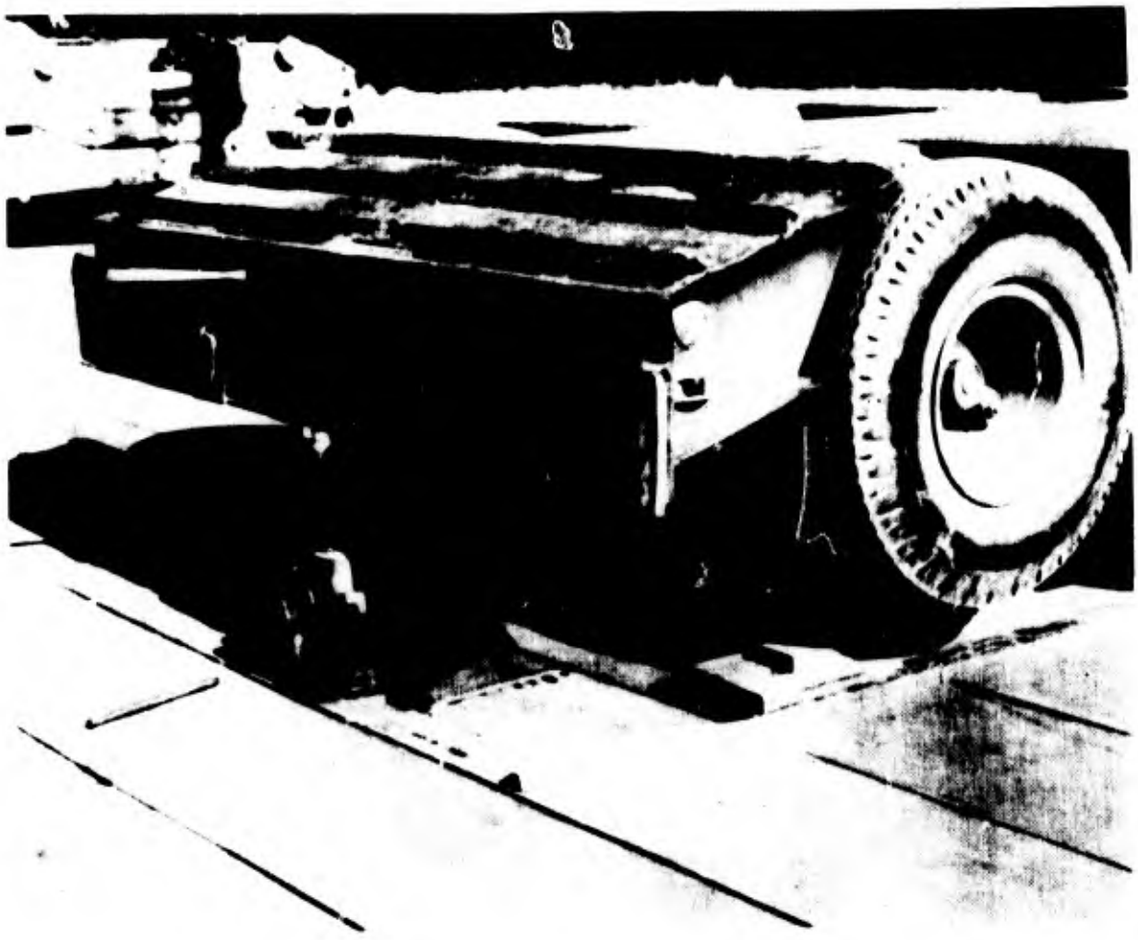

Figure 18. Equipment used for load testing.

One type of testing consisted of applying a harmonic, vertical loading to the soil or pavement surface and recording the velocity-phase characteristics of the transmitted waves. These wave characteristics were measured by means of accelerometers placed on the pavement surface at specified distances away from the vibrating load.

The second type of nondestructive test consisted of applying a relatively high amplitude vibratory load to the pavement surface by means of the hydraulic loading system shown in Figure 22 and recording the peak dynamic reflections. By plotting measured wave velocities versus wave length and consulting similar curves based upon elastic solutions, it is theoretically possible to select appropriate values of elastic response parameters for up to at least three layers. This provides a measure of the dynamic subgrade modulus of the composite pavement-subgrade profile.

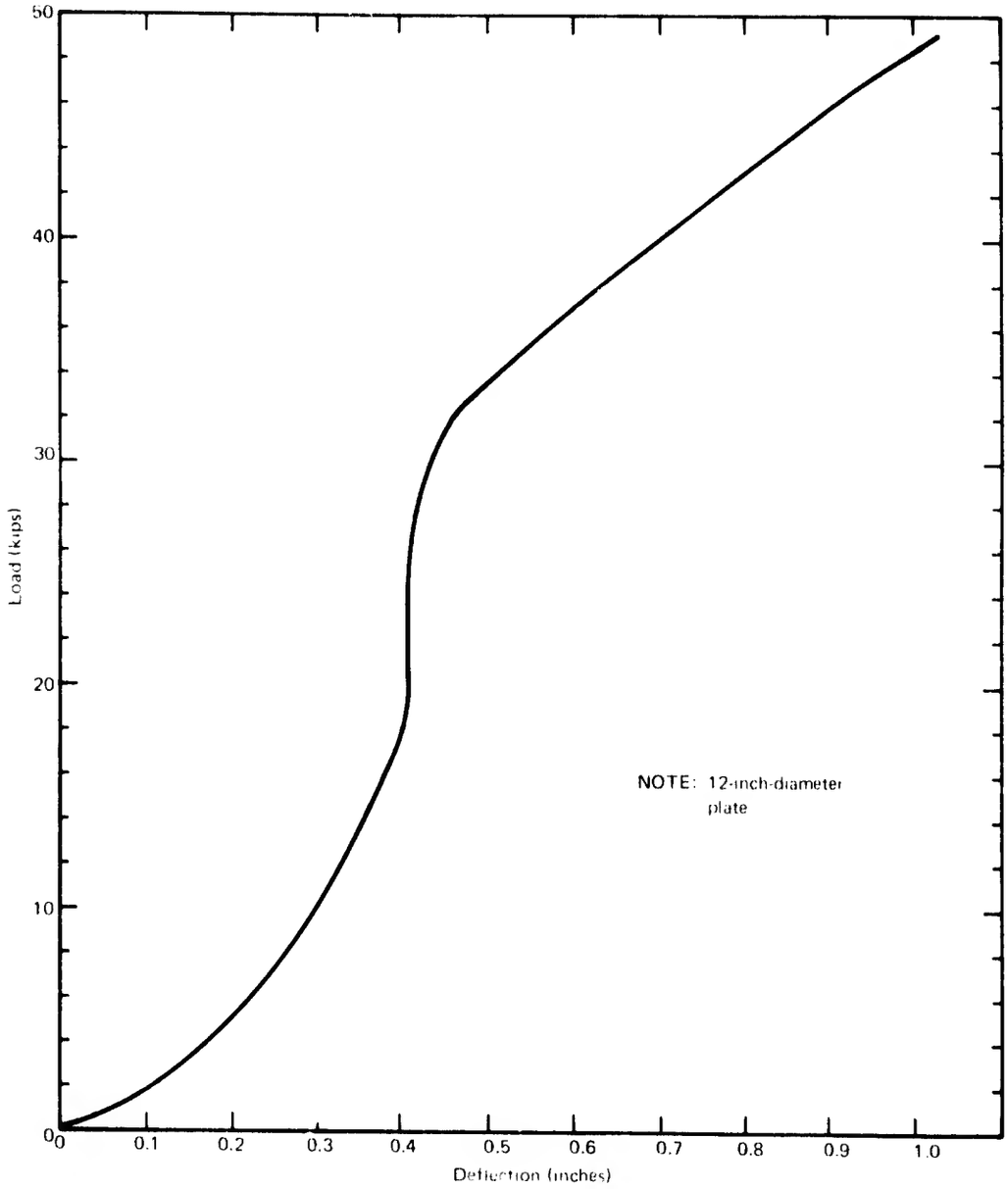

Figure 19. Plate-load response on AM-2 matting.

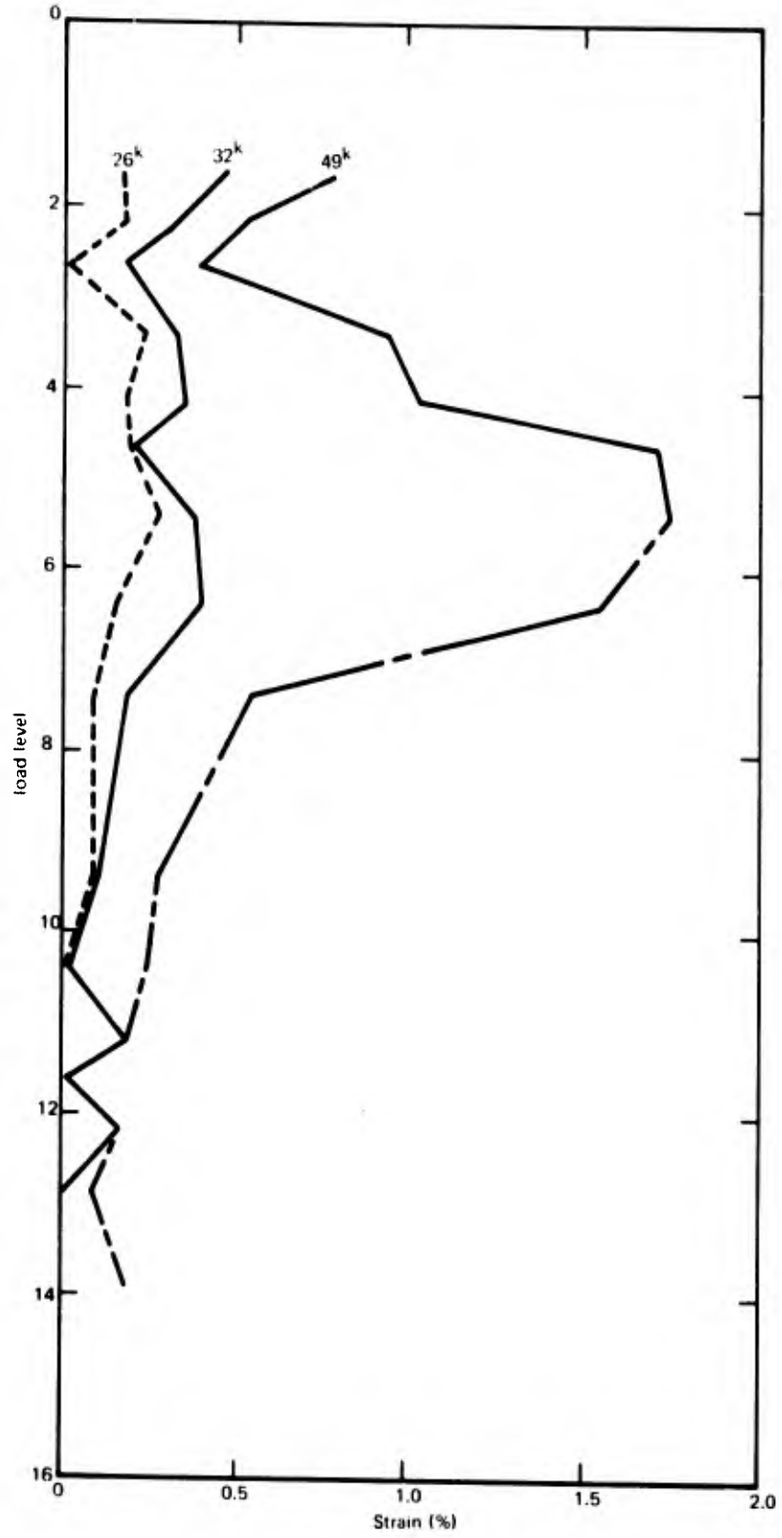

Figure 20. Vertical strains during plate-load tests on AM-2 matting.

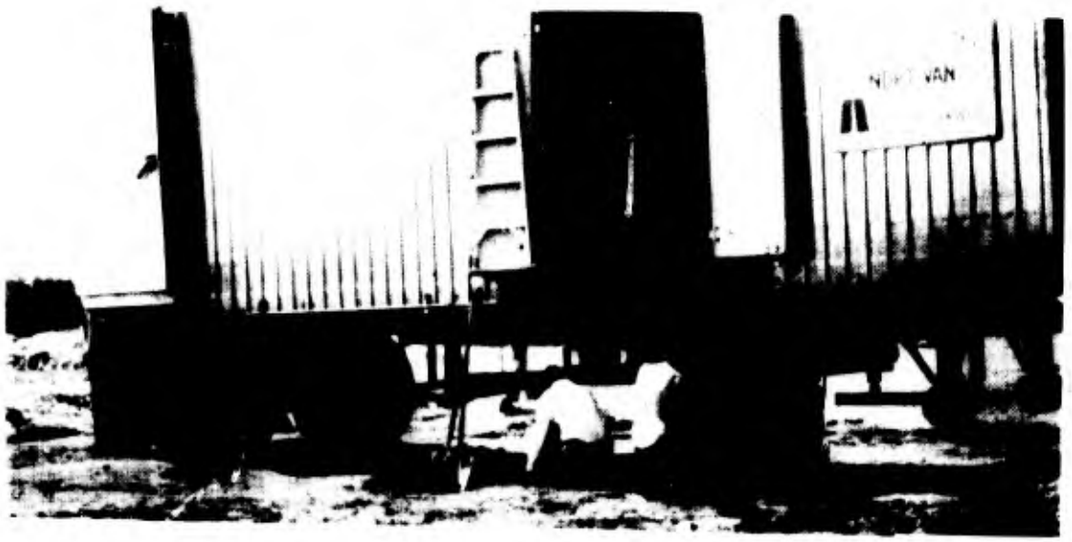

Figure 21. Nondestructive load testing van.

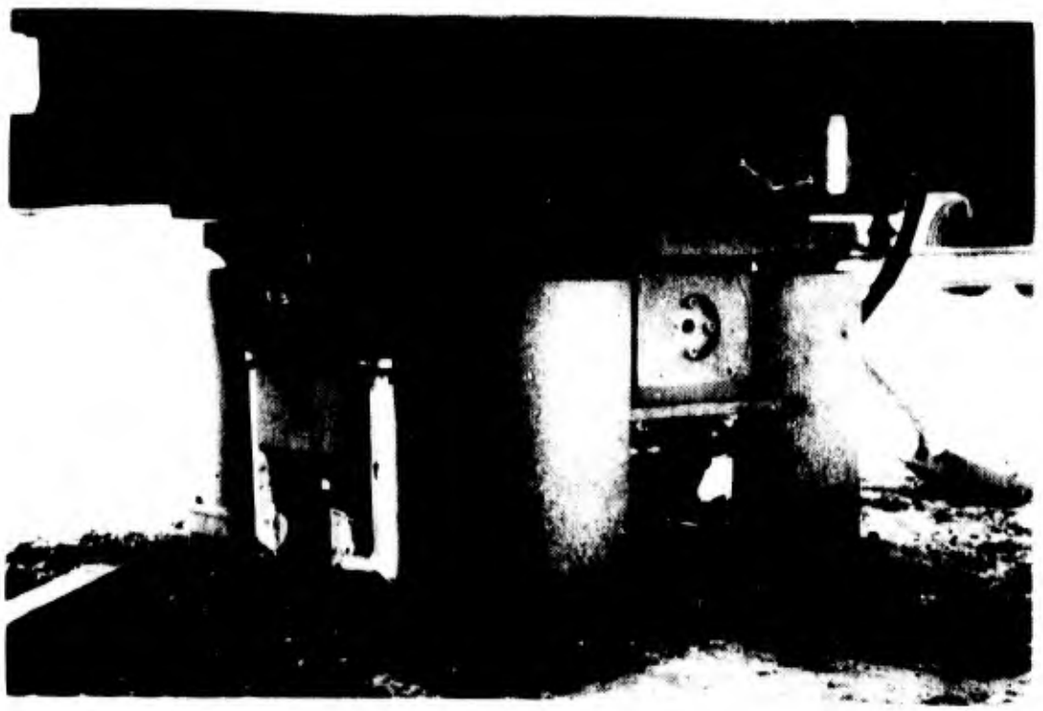

Figure 22. Vibratory load application.

The NDT equipment was designed for testing idealized plane systems, notably pavements; unfortunately, the repaired bomb craters did not meet this situation very well. The AM-2 matting used to surface the repaired crater was quite thin (1-1/2 inches thick) and poorly interfaced with the underlying base material. In addition, the backfill material beneath the base was extremely irregular and of the form of an inverted cone. For these reasons interpretation of the NDT data is somewhat questionable.

Another difficulty in interpreting the NDT data is that the shear modulus, G, is measured at extremely low shear strains. Reference 12 provides a means of modifying the value of the shear modulus to correspond to various shear strain levels. However, this reference provides no indication of the influence of shear strain on bulk or volumetric response. Since soils are known to be extremely dilatant (i.e., change in volume under applied shearing stress) and since volumetric strains could contribute a major portion of the surface deflections, this is a serious limitation for the present application.

Because of the foregoing difficulties, some inconsistencies were encountered in the interpretation of the NDT data. A detailed analysis of the nondestructive data must await presentation at a later date. At this stage, only a summary of the material data recommended in Reference 13 is presented in Table 5; this data is based on "best fit" of the results from various nondestructive tests. Since nondestructive testing is based upon the assumption of linear elastic behavior, only one value for each elastic parameter is determined. The parameters used in Table 5 are Young's modulus and Poisson's ratio; other elastic parameters, such as shear modulus, G, or bulk modulus, K, can be calculated from the basic elasticity relationships.

Table 5. Nondestructive Parameter Values (Reference 13)

Structure	Material	Young's Modulus, E (psi)	Poisson's Ratio, ν
Pavement as constructed	Layer 1	2.5×10^6	0.2
	Layer 2	0.25×10^6	0.3
	Layer 3	56,000	0.4
Repaired crater	gravel base	47,000	0.3
	debris backfill	22,000	0.4

SECTION V

COMPARISON OF ANALYTICAL AND FIELD RESPONSES

1. MODEL CRATERS AT CEL

a. Description of Tests

The responses of the models of runway repair systems tested at CEL have been reported in Reference 1; a brief summary of these tests follows. The model craters were approximately 10 feet in diameter and 6 feet in depth and were excavated using conventional construction equipment. These craters were partially backfilled using debris generated during the excavations. The backfill was completed using either a uniform pea gravel or a well-graded 3/4-inch gravel. The gravel was placed in both loose (relative density about 20%) and dense (relative density about 80%) conditions. The backfill was load-tested both uncovered and capped with a 6-inch-thick portland cement concrete surfacing. Loads were applied at the center of the repaired craters through a circular steel plate with an area approximating the contact area of an F-4 tire imprint (about 110 square inches). These tests were designed to provide comparison data for the finite element analysis and to provide additional information on the load-bearing capabilities of conventional geologic materials when placed under less than ideal situations.

The responses of two of these models are included in this report for comparison with the computer analysis:

1. A compacted gravel backfill capped with a 6-inch-thick concrete surfacing
2. Loosely placed gravel backfill capped with a 6-inch-thick concrete surfacing

Since the gravel backfill, which consisted of either a uniform pea gravel or graded base material, behaved similarly when placed at similar densities and confined by a rigid concrete surfacing, the test results for both materials were considered together when making comparisons with the computations provided by the finite element code. The pavement responses used for comparison and

considered most pertinent were: (1) vertical strain profiles beneath the loaded plate, (2) deflection basin profile of the repaired crater surfaces, and (3) load-deflection response of the loaded plate.

b. Material Definition

For the model craters, five different types of material were considered in the analysis: (1) the granular backfill in dense condition (relative density equals 80%), (2) granular backfill in loose condition (relative density equals 20%), (3) the excavated debris backfill, (4) the surrounding (i.e., in-situ) soil, and (5) the concrete surfacing.

Because funds were not provided to accomplish materials testing, literature and laboratory data for similar materials were used to accomplish the finite element analysis. The soil data needed consisted of values of bulk modulus, K, and shear modulus, G, as functions of volumetric strain, ε_v. (These data correspond to the material model used in the WINDAX code, see Section III.4a.) The confined nature of the backfill and the stiffness of the concrete cap forced the response of the backfill material to be more dependent on volumetric response than on shear response, which vindicates usage of the WINDAX material model. The concrete was assumed to behave elastically, with $E = 3.1 \times 10^6$ psi, $\nu = 0.2$, and a tensile cutoff strength, σ_c, of either 0 or 150 psi.

Experimental values defining the volumetric and shear response of several granular materials and a silty clay have been presented in Reference 1. The material responses selected for the crater backfill materials were based largely upon this information. Difficulties in selecting appropriate material response characterizations from the laboratory work arose due to the lack of measurements at very low confining stress levels (i.e., less than 5 psi). In the field tests the stiff concrete capping distributed the applied loading over a large region, resulting in relatively small hydrostatic stresses in the backfill material. The debris material, which consisted of chunks of asphalt, and the surrounding in-situ soil were assumed to have properties stiffer than the granular material placed over them. This assumption was felt to be the best characterization possible without resorting to substantial material testing.

Not only was it difficult to measure the volumetric stress-strain values for the backfill material at low stress levels, but even the shape of the initial portion of the curve was open to question. The volumetric response for a soil must exhibit stiffening throughout the normal range of volumetric stress

levels, but there appeared in the tests of Reference 1 to be softening that occurred over a very small strain region near zero load. Because the response of the backfill material in this region controlled the overall response of the repaired craters, values of the response parameters for other materials were consulted, see References 12, 14, 15, 16, and 17. Most of these references and particularly the work of Hardin (Reference 12) gave soil response data in agreement with the experimental laboratory work reported in Reference 1. On the basis of these references and the work reported in Reference 1, material characterizations for the backfill materials, in both loose and dense states, were selected. They are shown in Figures 23 through 26*.

Figures 23 and 24 show volumetric and shear response, respectively, for use in analysis of the compacted model crater. The surrounding soil was assumed to be elastic. Figure 23 shows assumed volumetric stress/strain response for the surrounding soil and for two states each of the gravel backfill and debris [i.e., preliminary and final: where the preliminary one was based largely upon the laboratory study (Reference 1) and the final characterization was a modification of the preliminary one in accordance with other work, including Reference 13.] Figures 25 and 26 show volumetric and shear response relationships, respectively, for use in analysis of the uncompacted model crater. Again the parameters of the surrounding soil were unknown, so they were assumed to be elastic. Because of the low stress levels reaching the in-situ soil, little advantage would be obtained by using a nonlinear relationship. The ''final'' material characterizations were used to specify the material properties for comparison of the analytical and measured responses.

c. Preparation of Finite Element Model

In providing verification of the computer model it is necessary to investigate the sensitivity of the model to various inputs; the model should exhibit small differences of behavior for relatively small variations of the input data. Some of the variables to be considered are: size of the finite element grid, number and density of elements, material volumetric and shear stiffness, limitation of tensile stress within an element, and number of load steps to be used in simulating the nonlinear structural response. A limited number of analytical results will be shown to provide some indication of the sensitivity of the model to reasonable variations in input data.

*Figures 24, 25, and 26 are on a foldout and appear at the end of this report.

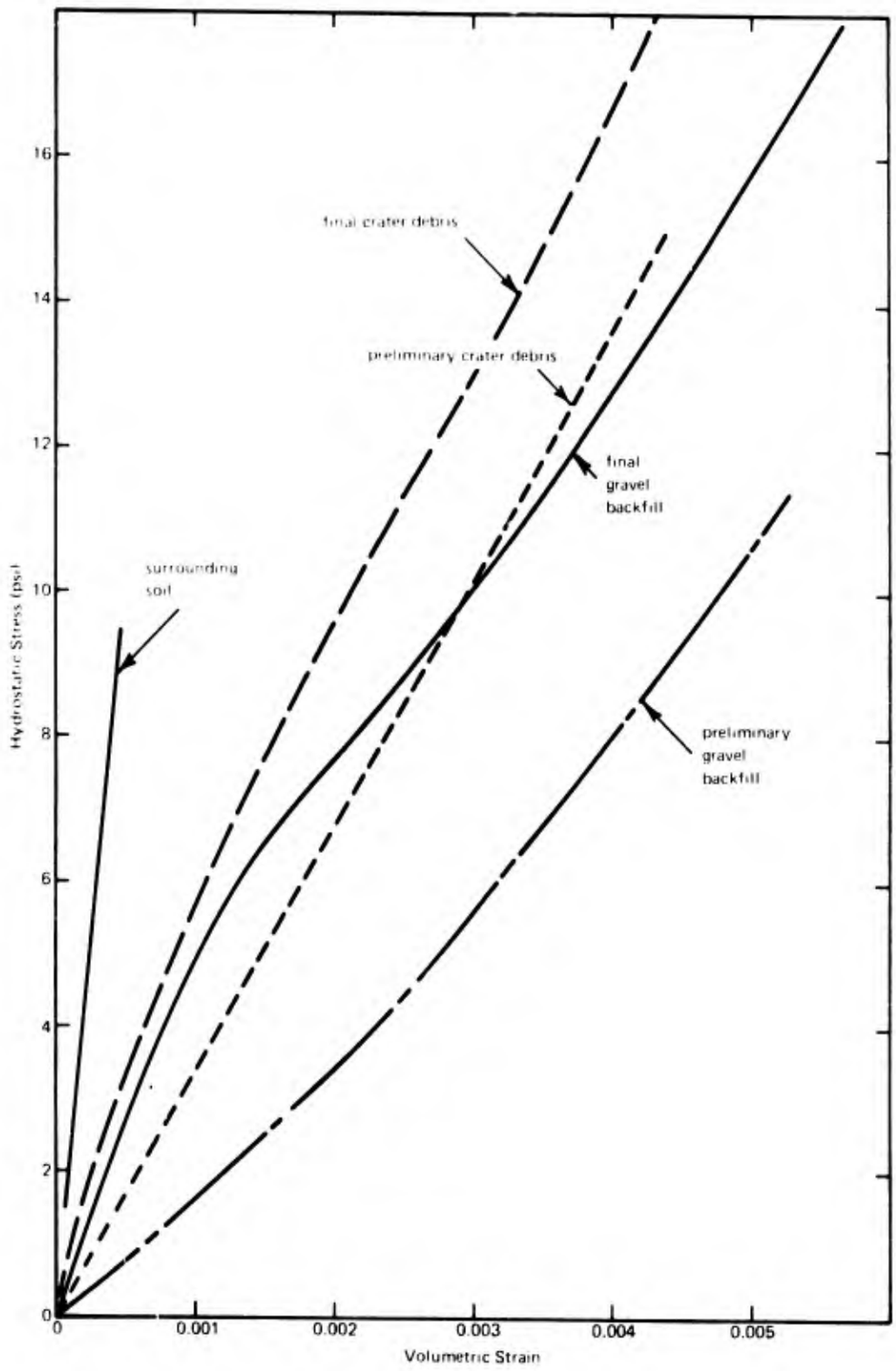

Figure 23. Material volumetric response for analysis of compacted model crater.

Assuming the finite elements for this code are roughly square in cross section and no more than an order of magnitude different in size, any reasonable grid selection should provide a reasonable answer. The major considerations become the number and size of elements and the overall dimensions of the structural section being simulated. These considerations are largely influenced by cost; that is, a compromise must be made between the degree of accuracy or definition desired and the cost of the computations. In the development of this computer code a number of different meshes were investigated. In these meshes the crater cross section is composed of four distinct materials: the concrete surfacing, the granular backfill, the replaced crater debris, and the surrounding soil. Figure 27* presents four meshes, with Figure 27e being the one finally selected. This mesh, composed of 598 elements, provided realistic simulation of crater response with ease of data generation and at reasonable cost (about 2 minutes of CDC 6600 time per run).

For purposes of model verification and sensitivity analysis, three quantities were considered: (1) the settlement of a loaded plate located over the center of the repaired crater; (2) the surface deflection basin surrounding the plate at an applied loading of 30 kips (approximately an F-4 wheel load); and (3) the vertical strain profile beneath the center of the loaded plate in the granular backfill. The first two quantities were selected because they determine the suitability of the crater repair; these quantities represent the summation of all the various material responses. The third quantity, vertical strain, is relatively unaffected by soil response occurring away from the area of measurement. This makes the measurement of strains extremely valuable to the validation of the analytical techniques which produce responses only as accurate as the material input. Only the material properties of the concrete and gravel are relatively well known, while the debris and in-situ material are based on best estimate. Thus, it is expected that the strain comparisons, which are dependent primarily on the concrete and gravel, will be closer than those of deflection, which are dependent on the entire soil mass. Based on similar arguments the shape of the analytical and experimental deflection curves will compare more favorably than the magnitudes, the magnitudes being affected by contributions from every material in the structure as well as the placement of the structure's boundary.

*Figure 27 is a foldout and appears at the end of this report.

d. Comparison of Test and Computer Results for Dense Backfill

Plate deflection/basin and vertical strains are compared in Figures 28, 29, and 30 for the compacted model crater. Analytical responses are shown for two different analyses. One analysis, computer run no. 87, used five increments of loading, while computer run no. 90 used 20 increments of loading. In situations such as this where deformations are reasonably small, using five loading steps provides response data that differs very little from a more lengthy analysis comprising 20 load steps. Figures 28 and 29 indicate calculated deflections that are larger than the measured ones. Figure 30 indicates calculated vertical strains that agree with the experimental ones over the major portion of the region of measurement. The divergence between the measured and the calculated vertical strains immediately beneath the concrete surfacing could suggest difficulties in measuring the strains in this region but are probably due to lower material densities achieved in compacting the unconfined backfill surface. Since measured and calculated vertical strains are in reasonable agreement, the excessive calculated deflections in Figures 28 and 29 must result from selection of response values for the underlying debris or surrounding soil that were too soft. No detailed experimental response data were available for these latter two materials; therefore, this latter conclusion is based upon assumption only.

Figures 31, 32, and 33 show comparisons of plate deflection, deflection basin, and vertical strain as calculated using both the preliminary and the final material input characterizations shown in Figures 23 and 24. Weakening the stiffnesses of the backfill materials had resulted in a large increase in vertical strains and a considerable increase in deflections. During the response calculations, deformations were found to be much more sensitive to variations in volumetric stiffness than to shear stiffness.

e. Comparison of Test and Computer Results for Loose Backfill

Figures 34, 35, and 36 present comparisons between calculated and measured values of plate deflections, deflection basin, and vertical strains, respectively, for the uncompacted model craters. The soil response relationships used for these calculations are shown in Figures 25 and 26. Figures 34 through 36 show the experimental responses and the results of three analytical simulations. The analytical response values illustrate the sensitivity of the computer code to number of load increments and permissible tension levels in the concrete.

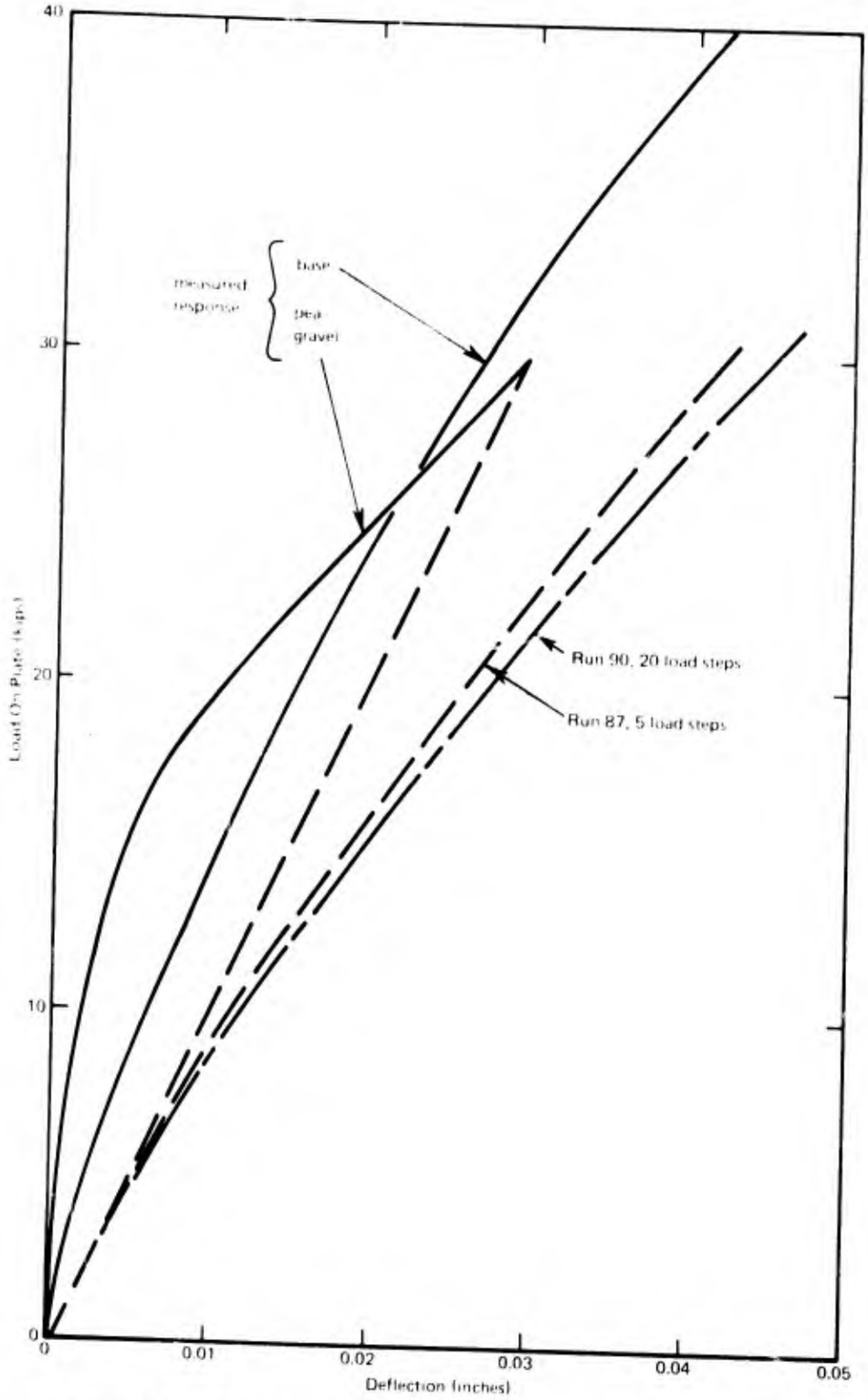

Figure 28. Plate-load response, compacted model crater.

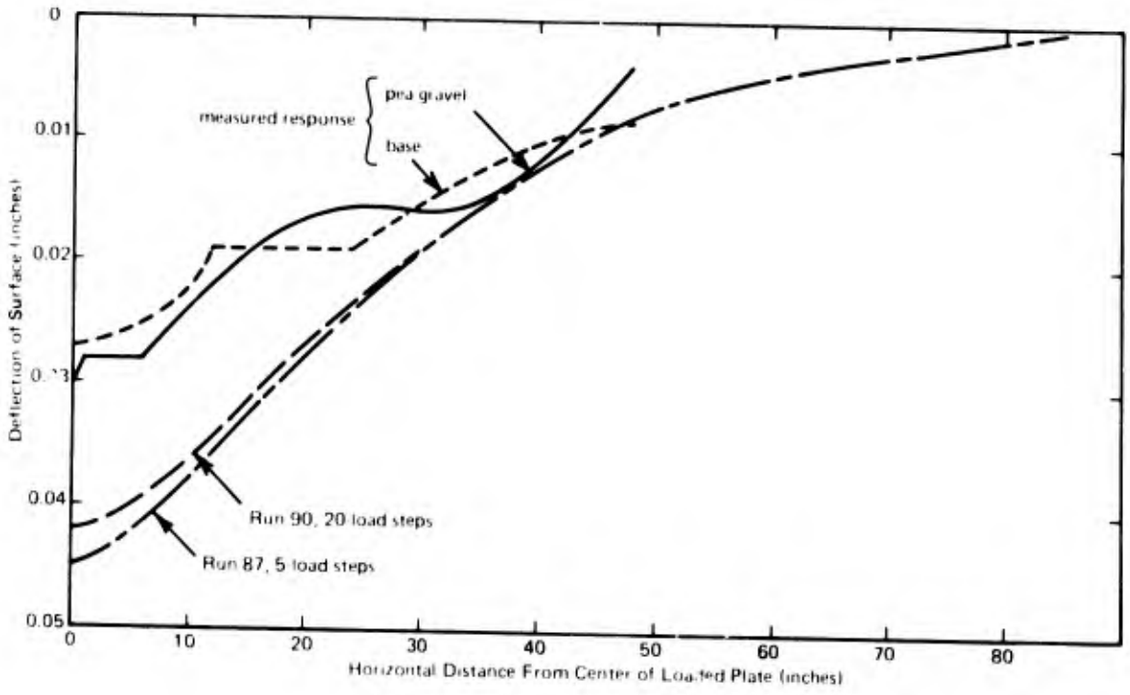

Figure 29. Deflection basins under 30-kip load, compacted model crater.

Computer runs 89 and 93 were similar, except that the concrete surfacing in run 89 was permitted to carry a maximum tension level of 150 psi before it cracked. In run 93, the concrete was not permitted to crack, and it developed a tensile stress level of approximately 1,050 psi. Large differences between the two analyses are evide in figures 34, 35, and 36. This clearly illustrates the shortcomings of using an elastic analysis to monitor structures that are approaching failure.

Figures 34 through 36 also indicate the influence of number of load steps on the calculated structural response. In computer run no. 89, the load of 30 kips was applied to the plate in five-load increments. Run no. 91 used 20 increments; otherwise, it was identical to run no. 89. Figures 34 through 36 show significantly increased deflections for run 91 as opposed to run 89, illustrating that a five-step solution is an inadequate approximation of the nonlinear response for this course. It is interesting to recall that in analyzing the response of the compacted model crater (Figures 28, 29, and 30) its stiffer and more linear response was modeled almost as well with five load steps as with 20 load steps.

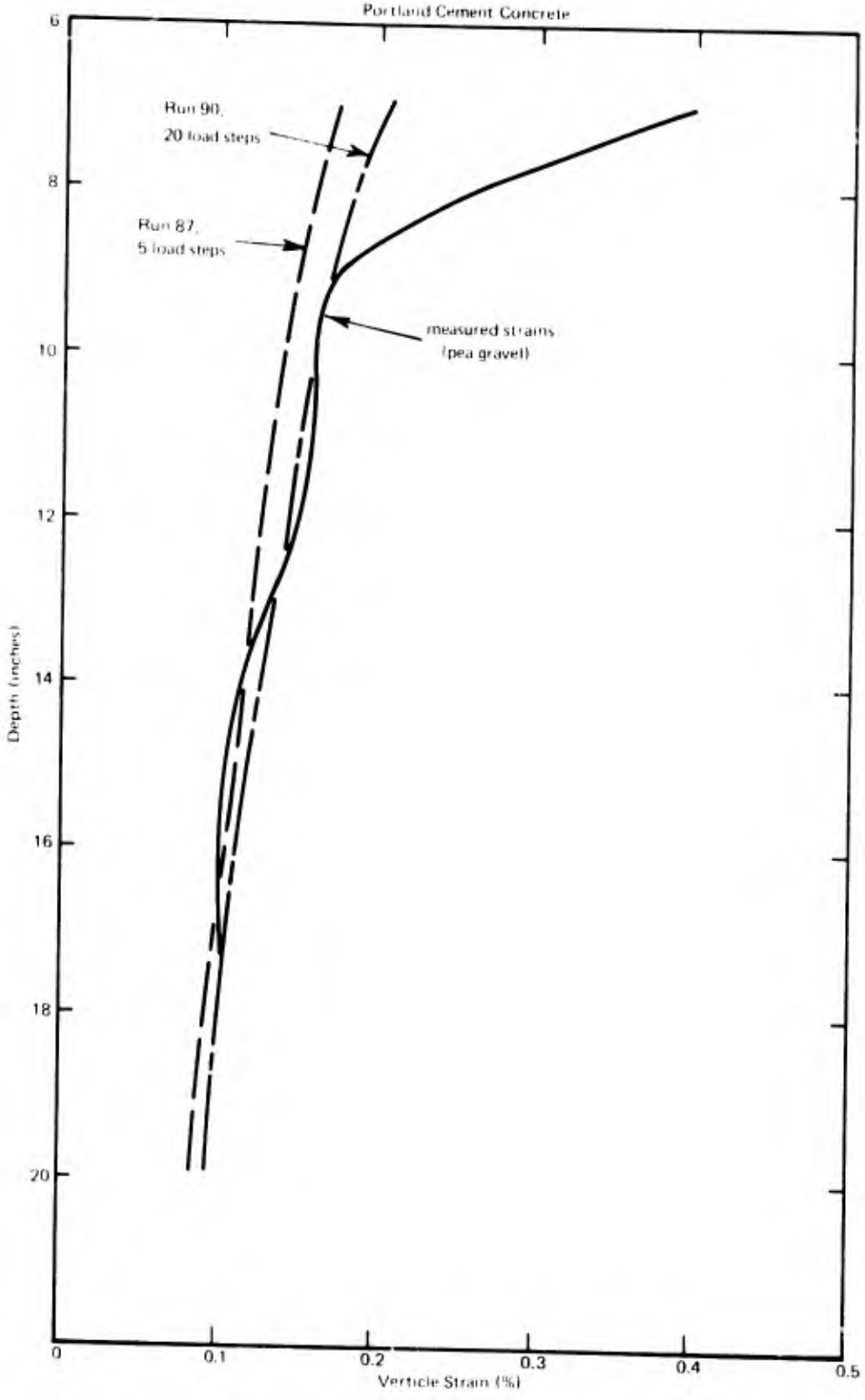

Figure 30. Vertical strains below plate under 30-kip load, compacted model crater.

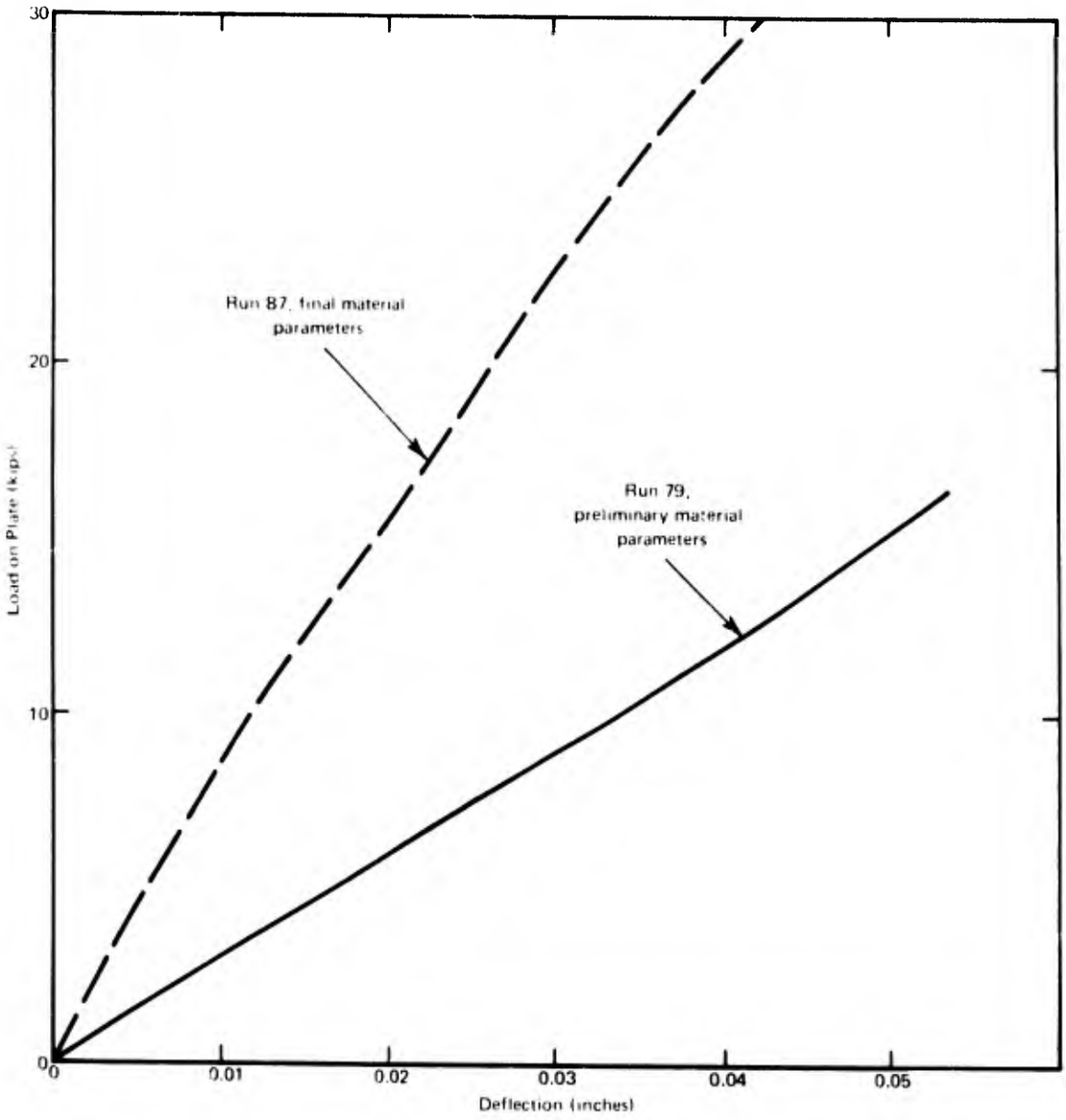

Figure 31. Comparison between calculated plate deflections, compacted model crater.

The analytical plate deflections from run no. 91 agree with the measured experimental values for the pea gravel backfilled crater at a load level of 30 kips. However, the shapes of the curves differ significantly. The experimental curves in Figure 34 show a distinct softening of the crater responses, particularly the one filled with base course material, near a load of 25 kips. This anomalous behavior arises largely because of physical difficulties in conducting the plate-load tests. At higher loads, the plate tends to tilt, causing concentrated forces under one edge. This not only increases the deflection of the

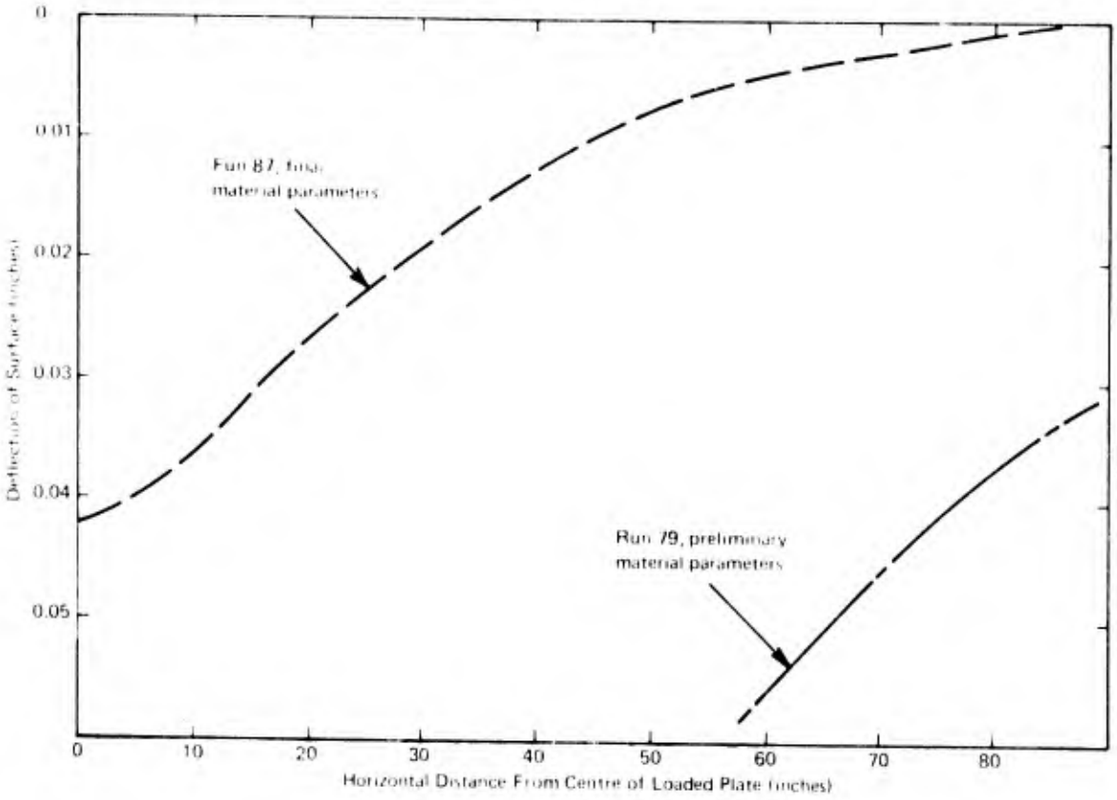

Figure 32. Comparison between calculated plate deflections, compacted model crater.

nonlinear material but initiates progressive failure beneath the loaded surface, thereby further increasing deformation. The finite element computer analysis, on the other hand, treats an axisymmetric solid and intrinsically prohibits any plate tilting and asymmetric stress concentrations. Agreement between analytical and experimental results is shown in Figure 35 for the deflection basins. At distances beyond 60 inches from the center of the loaded plate there are some discrepancies. This is because the edge of the concrete surfacing in this region separated from the underlying material by raising up during the centrally applied loading. This detail was not incorporated into the computer model.

The vertical strains depicted in Figure 36 show considerably more nonlinearity for the experimental strain profile as opposed to the analytical profile of computer run no. 91. This could be largely due to irregularities in placement of the backfill, the lower regions having received a greater degree of compaction during placement of the overlying layers. However, it is more likely due to the imprecise nature of modeling the properties of a loosely compacted soil using the WINDAX material law, which plays down the effects of shear, and to the lack of laboratory and literature data pertaining to the response of uncompacted soils.

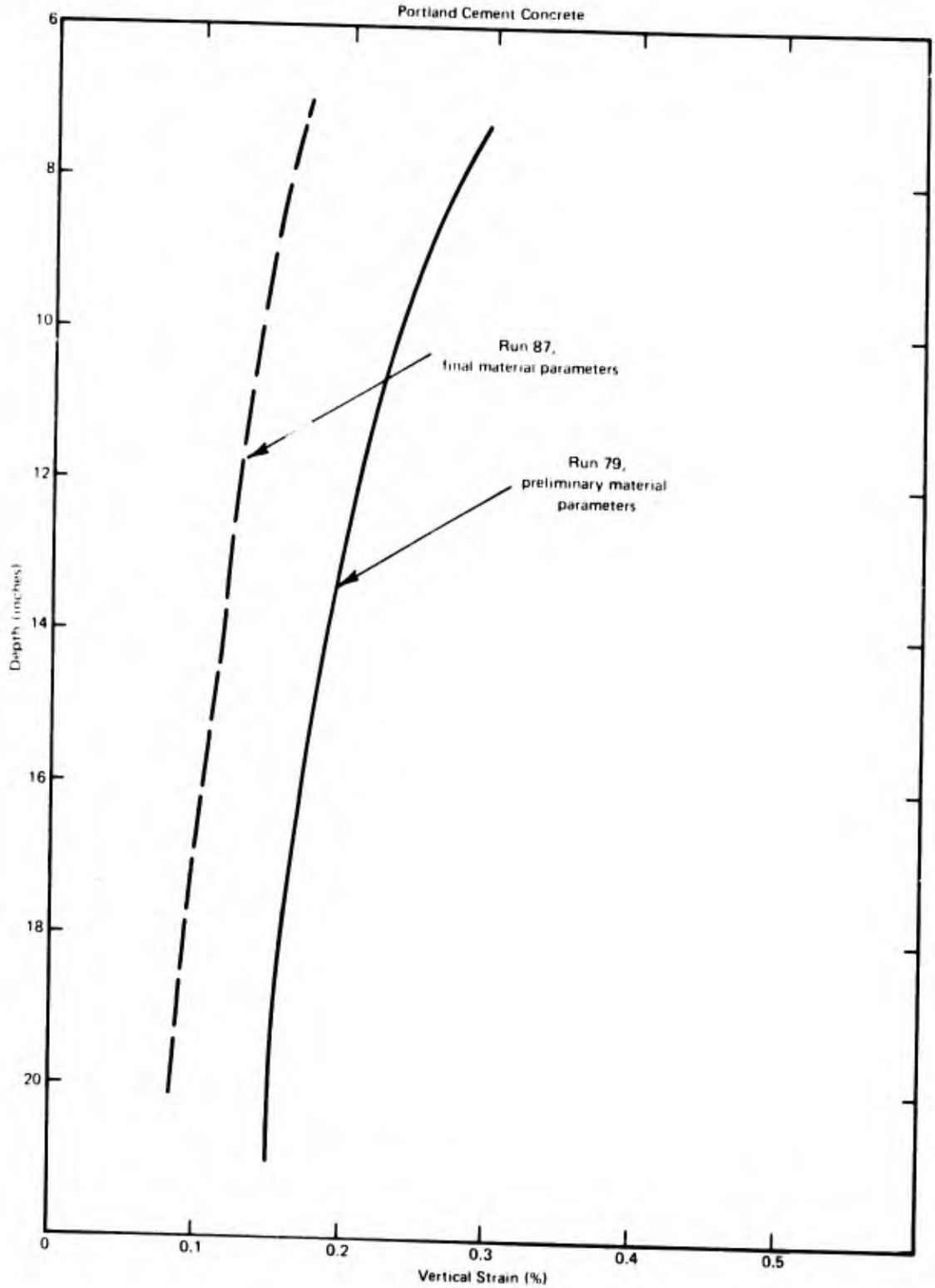

Figure 33. Comparison between calculated vertical strains, compacted model crater.

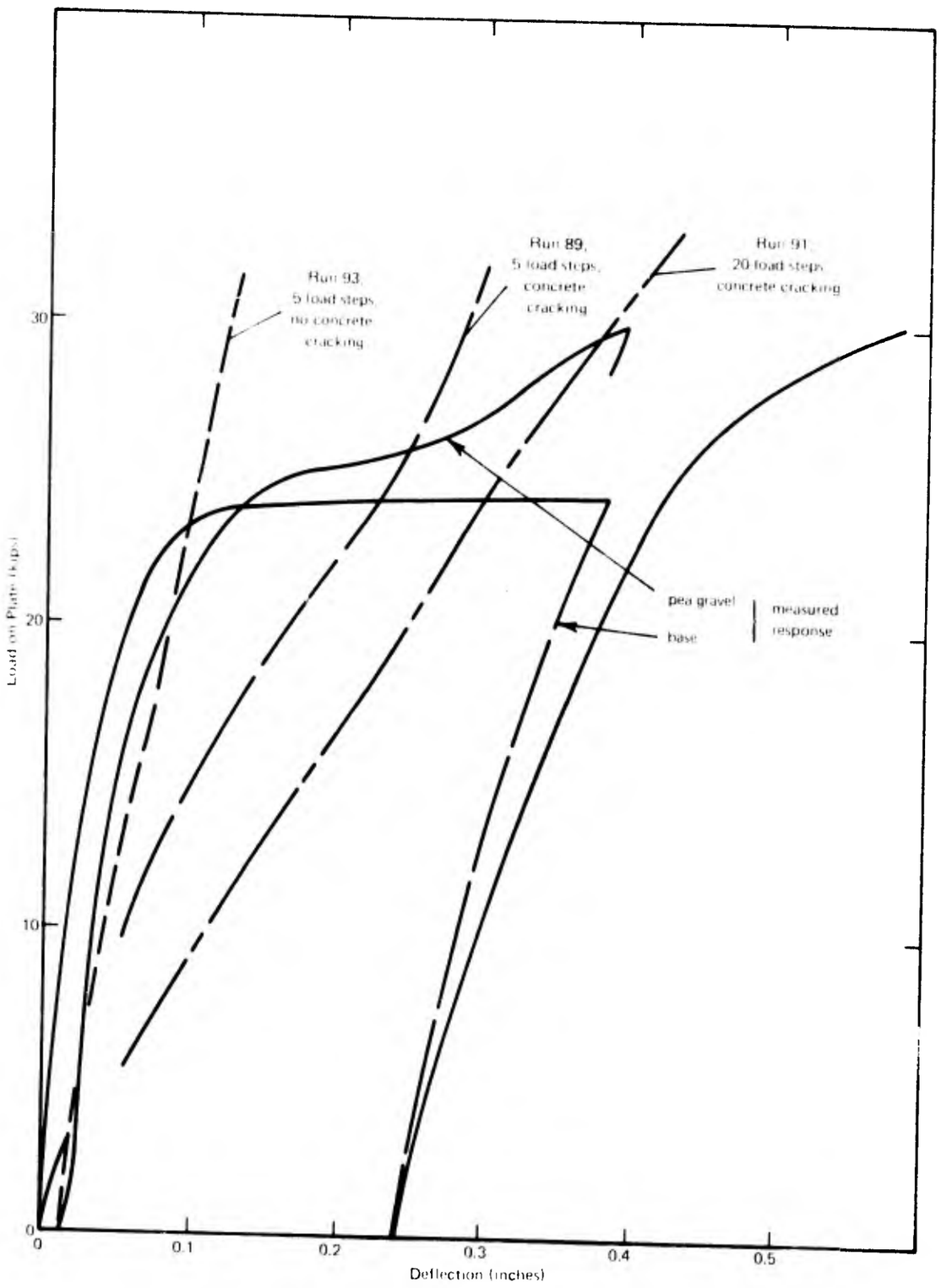

Figure 34. Plate-load response, uncompacted model crater.

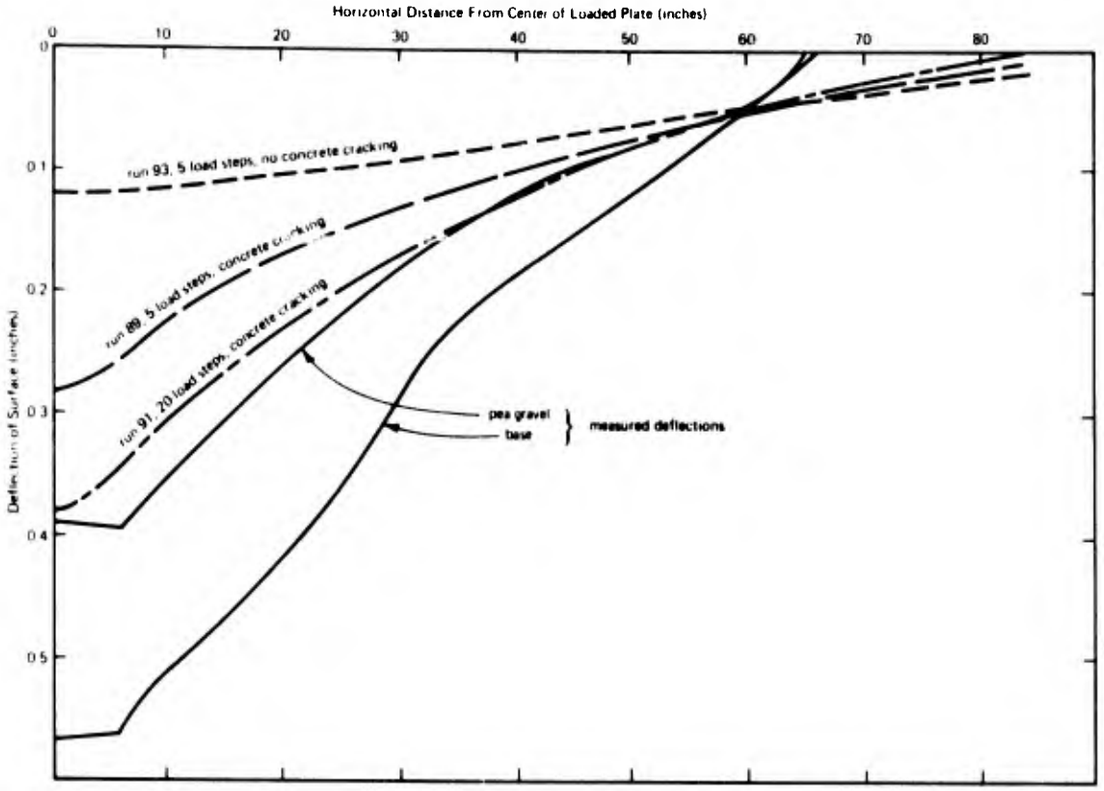

Figure 35. Deflection basins under 30-kip load, uncompacted model crater.

2. TYNDALL FIELD TESTS

a. Material Definition

The different materials encountered in the Tyndall field tests include: the AM-2 aluminum landing mat, the native fine sand, the crater wall and surrounding material, the granular base material, and the various types of crater debris. Section IV.3 provides descriptive field data on the various zones of crater debris material. Additional soil response data have been presented in Section IV.4. It was originally planned that AFWL would provide laboratory stress/strain measurements for specimens taken from the Tyndall test site; however, this was not accomplished. Thus, CEL was obliged to derive soil parameter values on the basis of index tests, field tests, and the literature. Material characterizations for the various materials are discussed below.

(1) AM-2 Matting. The AM-2 matting is an extruded aluminum matting, with an orthotropic structure, i.e., different structural characteristics in three major directions. To make the analysis of this material compatible with the

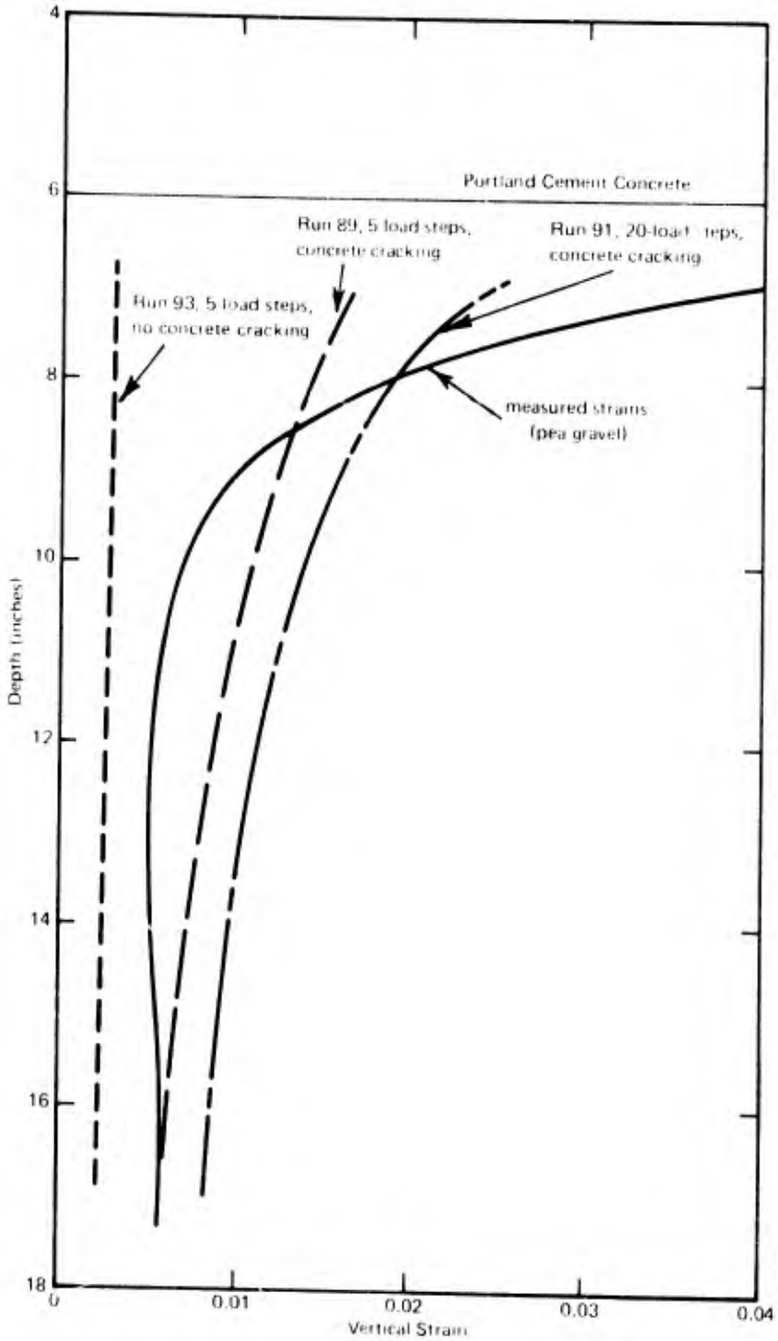

Figure 36. Vertical strains below the plate under 30-kip load, uncompacted model crater.

axisymmetric computer model, without introducing undue complexity, the matting is considered as an elastic, homogeneous material by giving it constant average values for its material properties in all directions. Based upon the stiffness properties suggested by the manufacturer for bending in the two major directions, the average elastic material properties are:

bulk modulus, $K = 2.22 \times 10^6$ psi
shear modulus, $G = 1.46 \times 10^6$ psi

(2) Native Florida Fine Sand. No information is available on the constitutive behavior of the Florida sand. The sand location is far enough from the applied line load that its behavior could be assumed linear. Based upon the laboratory studies conducted in conjunction with the model crater tests, index tests, and the literature (References 15 through 18), the following parametric values were selected:

bulk modulus, $K = 14{,}000$ psi
shear modulus, $G = 10{,}000$ psi

These values are representative of those measured on the CEL test sand (Reference 1). Similar values were also derived from Hardin's work (Reference 12) by assuming a Poisson's ratio for the sand of about 0.21, which is considered characteristic of drained sand under low stress levels.

(3) Crater Wall Material. This material was located largely outside the region of influence of the centrally applied live load. Since no constitutive data were available for it, it was assumed to behave similar to the native material.

(4) Granular Base Course Material. No laboratory data were available on the response parameters for this material. Thus, the CEL experimental studies, together with the index and field load tests, were used to predict the response parameter values. Widely divergent stiffness values were indicated by the static 30-inch-diameter plate-load tests and the nondestructive tests on both the gravel base and the backfill debris. Laboratory data generated by CEL and reported in Reference 1 indicate that the statically derived data were probably

much more applicable than the values measured in the nondestructive tests at very low stress levels. On the basis of available information, the parametric values shown in Figures 37 and 38 were selected for the granular base material.

The relationships shown in these figures fall within the experimental ranges measured in Reference 1. They could also be derived by using Hardin's relationships along with estimates of shear strain and Poisson's ratio. For example, consider the shear modulus values for the base course at a confining pressure (volumetric stress) of 10 psi in Figure 38. By using the average measured base course density of 135 lb per cu ft, Hardin's method (Reference 12) would predict values of shear modulus of 2,800 or 2,450 psi for shear strains of 0.16% or 0.18%, respectively. These numbers correspond to the respective modulus values at the 10-psi volumetric stress level shown by the curves for Runs 74 and 67. Using these values of shear modulus and selecting appropriate values of Poisson's ratio, the values of bulk modulus shown in Figure 37 are computed.

Where no experimental soil data exist for the material being analyzed, it is necessary to estimate material parameter values. Obviously experience is very valuable in this regard. However, an engineer without an intimate knowledge of soil mechanics should be able to ascertain reasonable input values for comparison purposes by referring to the literature, such as References 12 through 18. Reliance on literature data becomes inadequate for such unusual materials as debris and uncompacted granular backfills.

(5) Backfilled Debris. Due to the large variations occurring in this material, it would have been difficult to select representative parametric response values even if considerable experimental data had been available. As with the granular base material, the static plate-load tests indicated stiffness parameters an order of magnitude lower than those determined by nondestructive testing techniques. Since the only load response information available for this material were load tests, approximate ranges of material parameters were selected that would provide ''elastic'' deflections corresponding to the measured ones. The shapes of the actual stress/strain curves were then arbitrarily selected, based upon experience and a comparison of the available index data with that for other materials in the literature. Obviously this is not a satisfactory scientific procedure; nevertheless, it was appropriate for purposes of comparing different repair procedures.

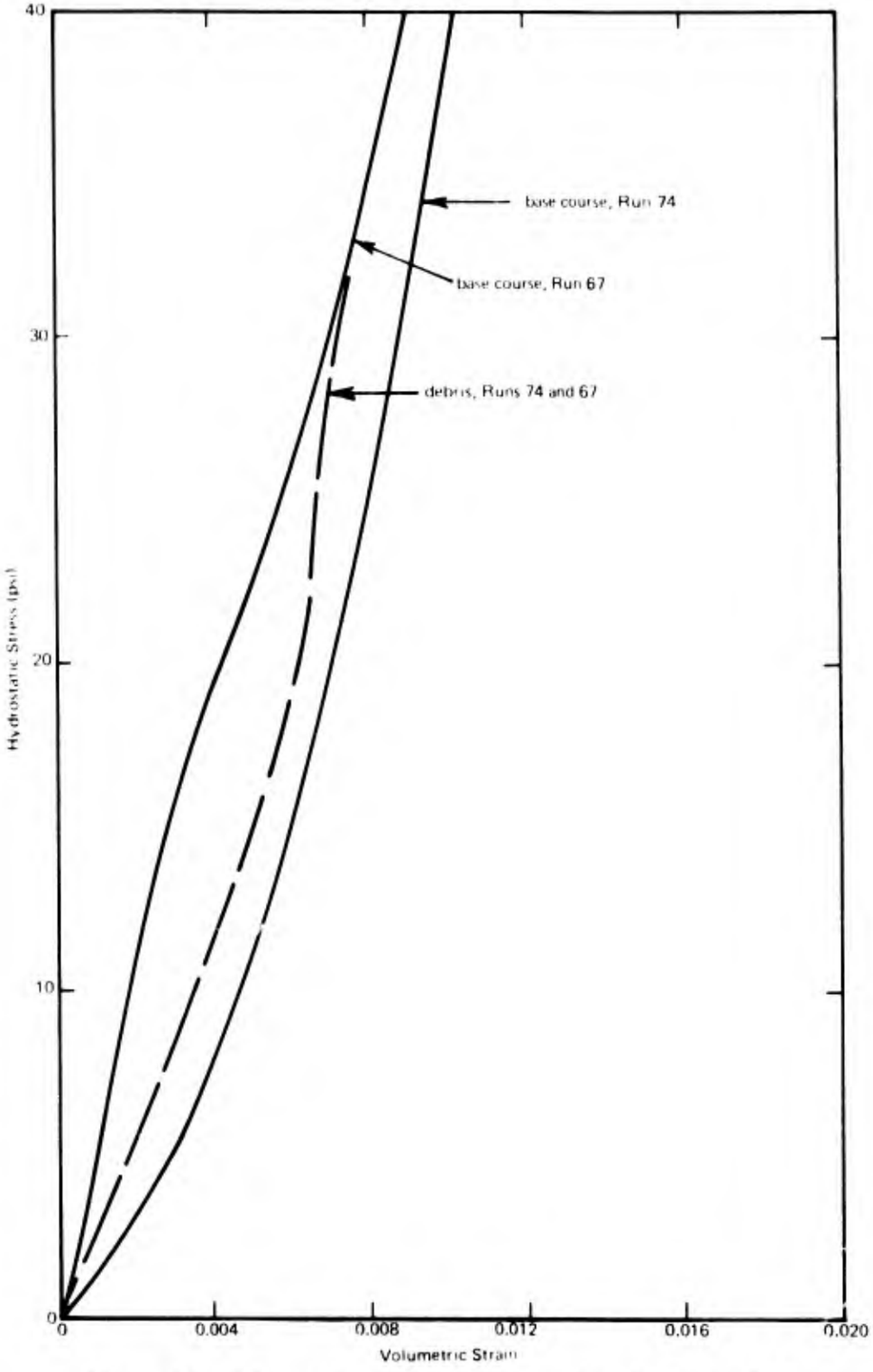

Figure 37. Volumetric response for crater 1-2 materials.

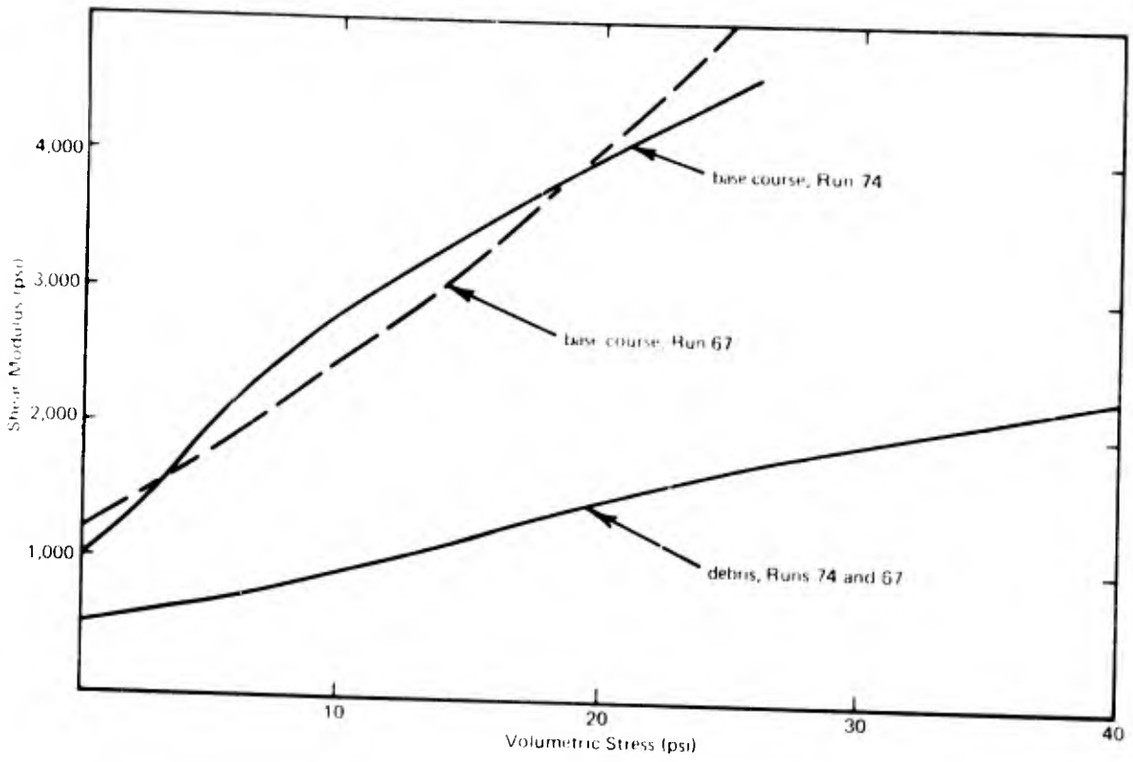

Figure 38. Shear response for crater 1-2 materials.

b. Comparison of Test and Computer Results

With curtailment of the materials testing portions of the project (which resulted in usage of ''best estimate'' materials input for WINDAX), code evaluations based upon the Tyndall field test are not possible. In addition, difficulties in measuring the surface profile and the resulting erratic data (see Section IV.4c) have impaired the usefulness of the plate-load tests, yielding questionable results for correlation with WINDAX. This has resulted in most of the emphasis being placed on the model test correlations (Section V.1) for validation of the computer code.

However, the comparisons presented in this section fulfill a useful function. The comparisons indicate that: first, the analytical response based on ''best estimate'' material properties is reasonably close to that measured; and second, that the ''best estimate'' material properties can be used to compare the various repair schemes with one another. Finally, these comparisons indicate the importance of materials testing, especially with respect to the debris material.

The finite element mesh used for analyzing crater 1-2 is shown in Figure 39. The material response parameters used for all the materials involved in the analysis of the crater have been presented in Section V.2a. For the two computer runs made, similar volumetric and shear responses were used for the debris, while the granular base material in computer Run 74 was somewhat softer than in Run 67 in the region of small confining stress.

Comparisons of plate-load response are shown in Figures 40, 41, and 42. Figure 41 shows plate deflections under load for the experimental case and the

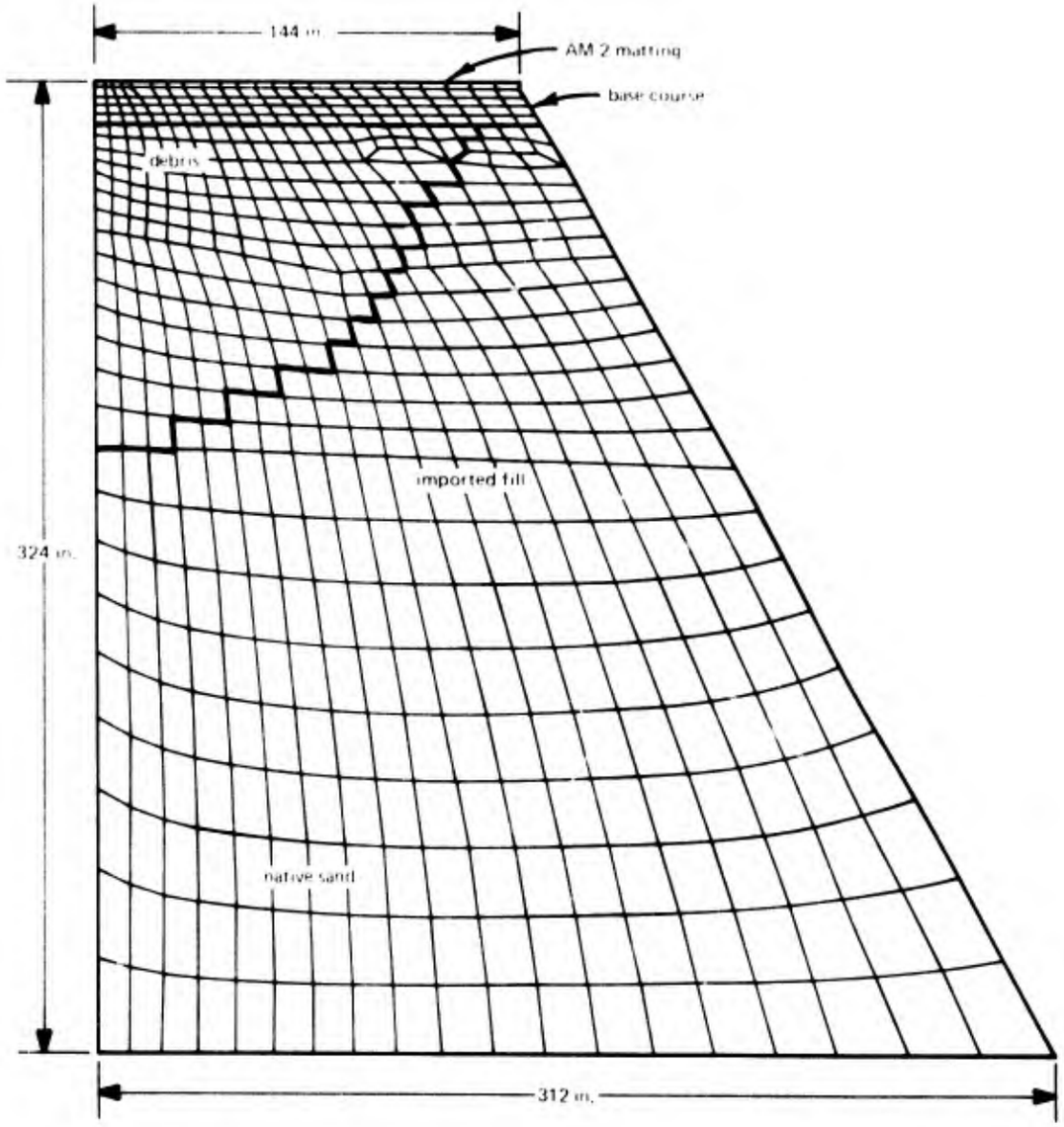

Figure 39. Finite element mesh used for analysis of crater 1-2.

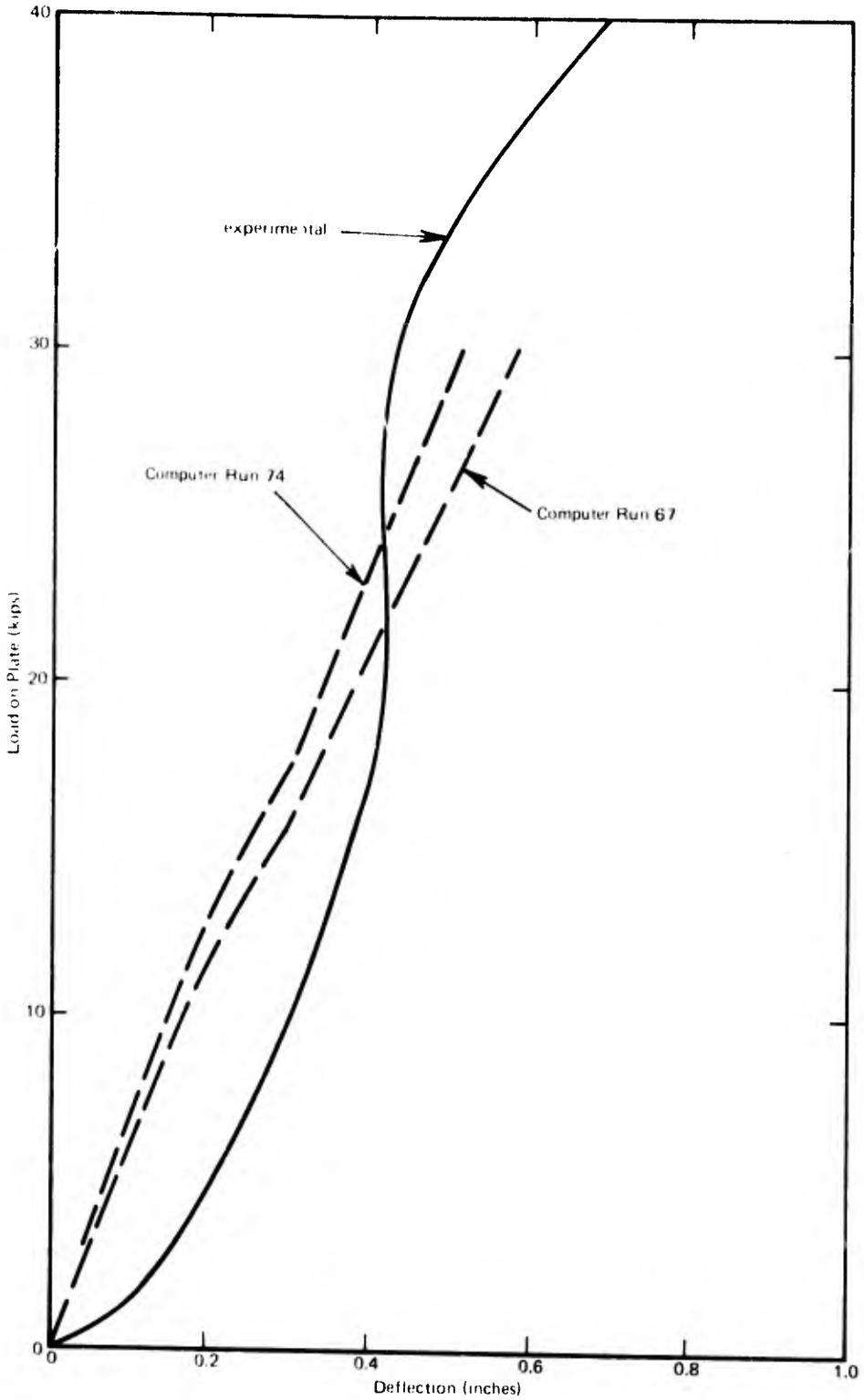

Figure 40. Plate-load response, crater 1-2.

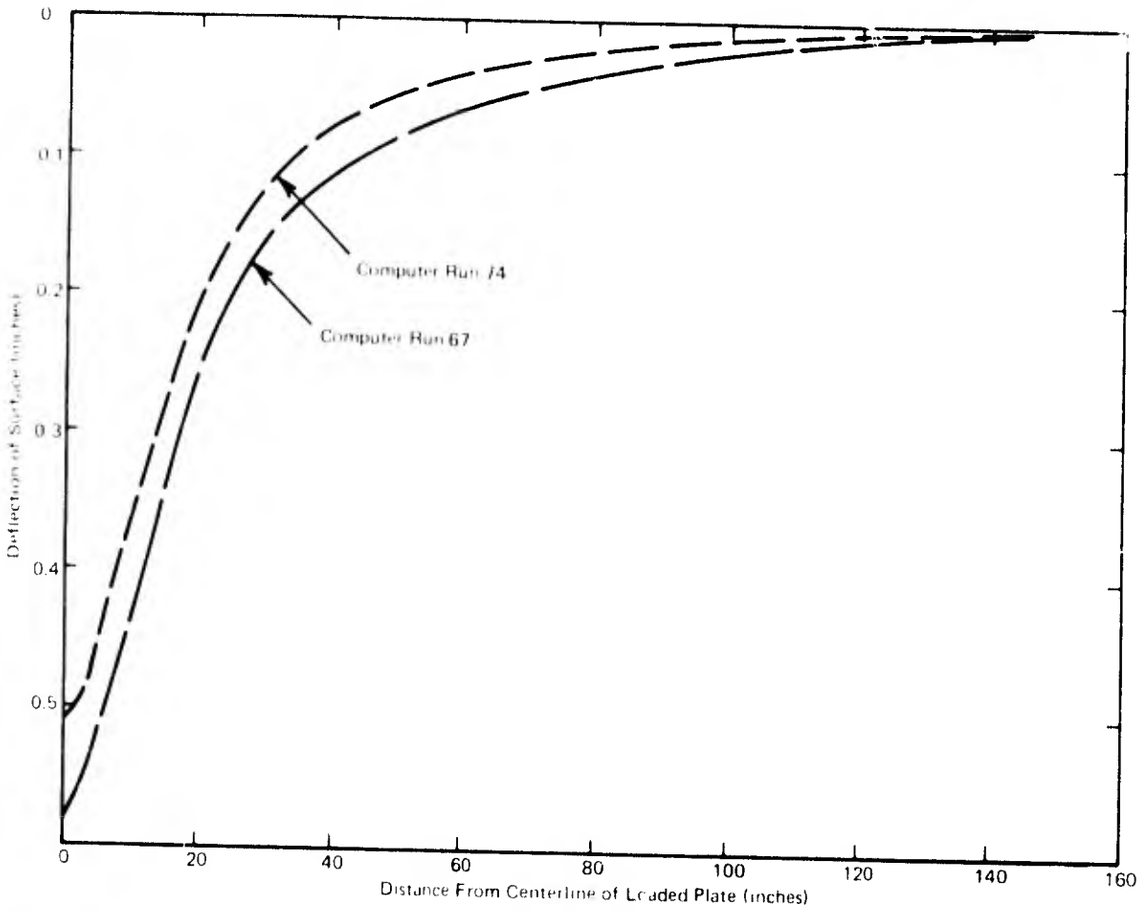

Figure 41. Deflection basins under 30-kip load, crater 1-2.

two analytical cases. Figure 41 shows deflection basins for the two computer runs. Because of the erratic behavior of the AM-2 matting, the measured surface profile is not reported. It is noted that a slight increase in gravel base stiffness, as shown in Figures 37 and 38, results in reduced deflections in Figures 40 and 41. A comparison of the calculated and measured vertical strains occurring beneath the centerline of the loaded plate at roughly similar loads is shown in Figure 42. Near the surface, where the backfill is relatively homogeneous and well compacted, the comparisons are close, while large discrepancies occur with greater depth.

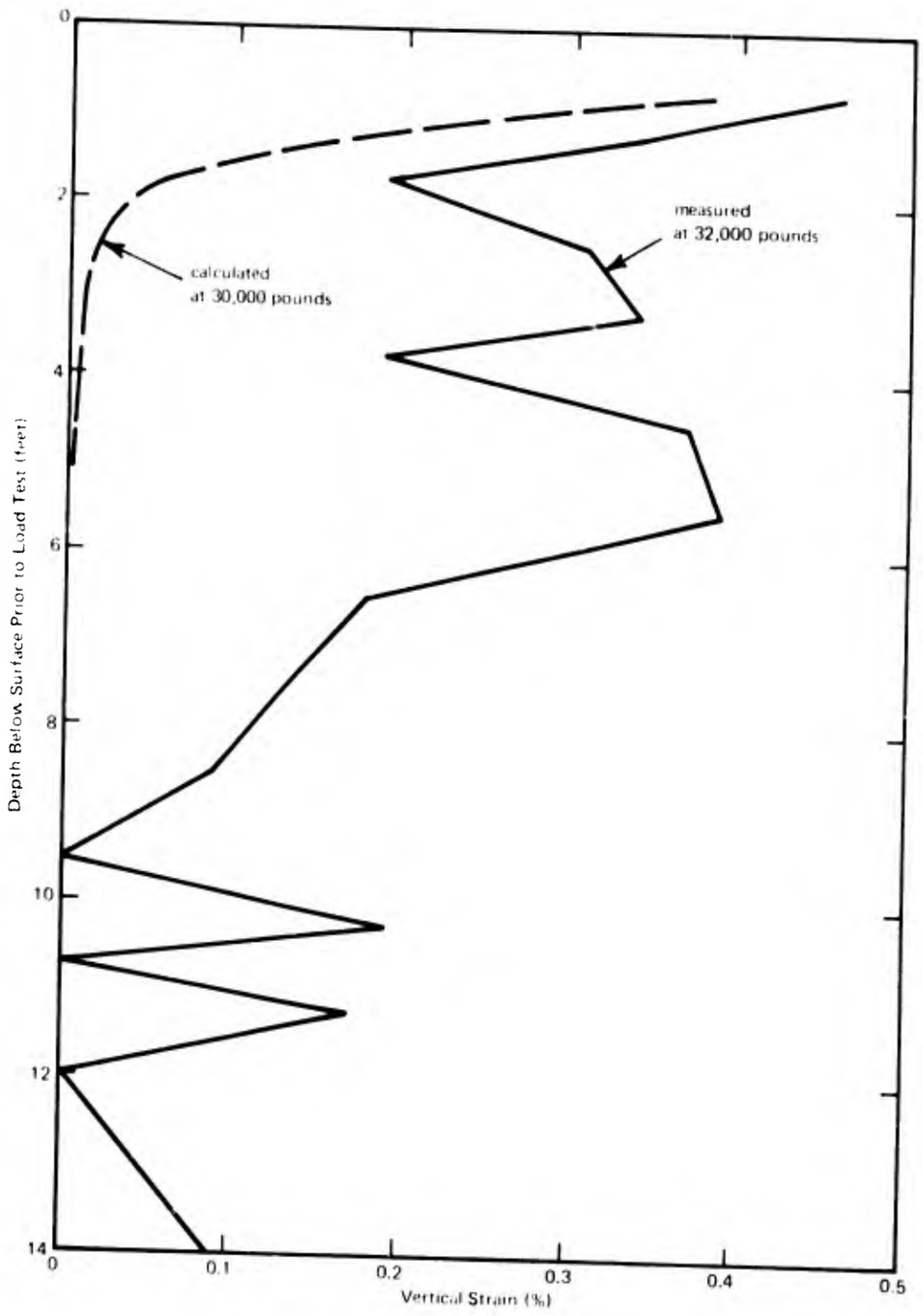

Figure 42. Vertical strains beneath plate centerline, crater 1-2.

It is possible to more closely approximate the measured results with the computer model by changing the material parameters. However, changing "best estimate" material properties so that the comparisons are more favorable has little merit unless this is based on more knowledge about the materials present in the repaired crater. The most significant problem encountered during these comparisons was the almost total lack of knowledge concerning the characteristics of the debris.

SECTION VI

CONCLUSIONS

A finite element computer model has been presented and shown to be capable of predicting the response of repaired craters to applied loadings. Comparisons have been made between analytical and measured deformations for both small-scale models and a full-size prototype repaired crater. The model crater tests were discussed in detail in Reference 1; only those model craters surfaced with 6 inches of concrete were included in the correlations for this report. The prototype crater was surfaced with AM-2 matting and, therefore, corresponds to the conventional Air Force recommended procedure for rapid repair.

An expedient method for carrying out laboratory evaluations of material input properties was presented in Reference 1. The present report utilizes the original laboratory data and also suggests additional sources of material input data in the literature, such as Hardin's method (Reference 12) or Duncan and Chang's method (Reference 15) that have proved adequate for use in defining soil properties for input to this code. For purposes of comparing different methods of crater repair, the material parameter values presented in this report are adequate.

The correlations between experimental and analytical responses were used both to validate the computer model and to provide some idea of output sensitivity. For example, four variations of the mesh for the CEL model crater are shown, and a discussion of mesh selection has been presented. The influence of the number of load steps was shown, and it is apparent that the more nonlinear the problem the more steps required. Comparisons of material stiffness to pavement deformation show that a change in material parameters results in reasonably similar differences in predicted response. However, the nonlinear response prohibits any one-to-one relationships. Permitting the cracking of the concrete cap was shown to be extremely important where large deformations are concerned.

In summary, a finite element computer code is presented that is capable of representing the response of repaired craters to applied loading with a degree of precision corresponding to the accuracy of the materials characterization. Where relative comparisons of the response of different repair procedures are required, the soil parameters presented in this report are applicable. In specific situations where other materials must be considered, appropriate literature is suggested for providing the required parameter definitions. Where

accurate predictions of the response of a particular repair method are required, a laboratory testing program, such as that defined in Reference 1 or suggested in References 12, 14, 15, or 17, is necessary.

REFERENCES

1. Forrest, J. B., and T. A. Shugar. A Structural Evaluation of Rapid Methods of Backfilling for Bomb Damage Repair, AFWL-TR-73-29. Air Force Weapons Laboratory, Kirtland AFB, NM, Mar 1974.

2. Air Force Manual 93-2. Change 1. Disaster Preparedness and Base Recovery Planning: Chapter 5, Rapid Runway Repair Procedures. Headquarters, Department of the Air Force, Washington, D.C., Jun 1970.

3. Zienkiewcz, O. C., and Y. K. Cheung. The Finite Element Method in Structural and Continuum Mechanics. McGraw-Hill, London, England.

4. Doherty, W. P., E. L. Wilson, and R. L. Taylor. Stress Analysis of Axisymmetric Solids Utilizing Higher-Order Quadilateral Finite Elements, Department of Civil Engineering, Report 69-3. University of California, Berkeley, CA, Jan 1969.

5. Naval Civil Engineering Laboratory. Technical Report R-789: Effect of Backpacking and Internal Pressurization on Stresses Transmitted to Buried Cylinders, by S. K. Takahashi. Port Hueneme, CA, May 1973.

6._____. Technical Report R-771: Summary of Soil-Structure Interaction, by J. Allgood. Port Hueneme, CA, Jul 1972.

7. Army Engineer Waterways Experiment Station. Contract Report N-70-1, A Nonlinear Finite Element Code for Analyzing the Blast Response of Underground Structures, by I. Farhoomand and E. Wilson. Vickburgs, MS, Jan 1970. (Contract DASA 39-67-C-0020)

8._____. Misc. Paper No. 4-980. Factors That Influence the Development of Soil Constitutive Relations, by J. G. Jackson. Vicksburg, MS, Jul 1968.

9. Hokanson, D., Tyndall AFB Bomb Damage Repair Field Tests, Documentation and Analysis, AFWL-TR-74-226, Air Force Weapons Laboratory, Kirtland AFB, NM, to be published.

10. Rao, H. A. B., and D. Harnage. Evaluation of Rigid Pavement by Nondestructive Tests, HR Record 407. Highway Research Board, Washington, D.C., 1972.

11. Selig, E. T., and J. Ho. Evaluation of Instrumentation for Soil Strain Measurement. Department of Civil Engineering, State University of New York, Buffalo, NY, Apr 1970.

12. Hardin, B. V., Effects of Strain Amplitude on the Shear Modulus of Soils, Air Force Technical Report No. AFWL TR-72-201. Air Force Weapons Laboratory, Kirtland AFB, NM, Mar 1973.

13. Personal Communication, H. A. B. Rao, Civil Engineering Research Facility, University of New Mexico, Albuquerque, NM.

14. Domaschuk, L., and J. H. Wade. ''A Study of Bulk and Shear Moduli of Sand.'' Journal of Soil Mechanics and Foundations Division, ASCE, Vol. 95, No. SM2, Proc. Paper 6561, Mar 1969.

15. Duncan, J. M., and Chin-Yung Chang. ''Nonlinear Analysis of Stress and Strain in Soils,'' Journal of the Soil Mechanics and Foundations Division, ASCE, Vol. 96, No. SM5, Proc. Paper 7513, Sep 1970.

16. Brown, S. F., and D. I Bush. ''Dynamic Response of Model Pavement Structure,'' Journal of Transportation Engineering Division, ASCE, Vol. 98, No. TE4, Proc. Paper 9363, Nov 1972.

17. Marachi, N. D., D. K. Chan, and H. B. Seed. ''Evaluation of Properties of Rockfill Materials,'' Journal of the Soil Mechanics and Foundations Division, ASCE, Vol. 98, No. SM1, Proc. Paper 8672, Jan 1972.

18. Arthur Penman and Andrew Charles. ''Constructional Deformations in Rockfill Dams,'' Journal of the Soil Mechanics and Foundations Division, ASCE, Vol. 99, No. SM2, Proc. Paper 9560, Feb 1973.

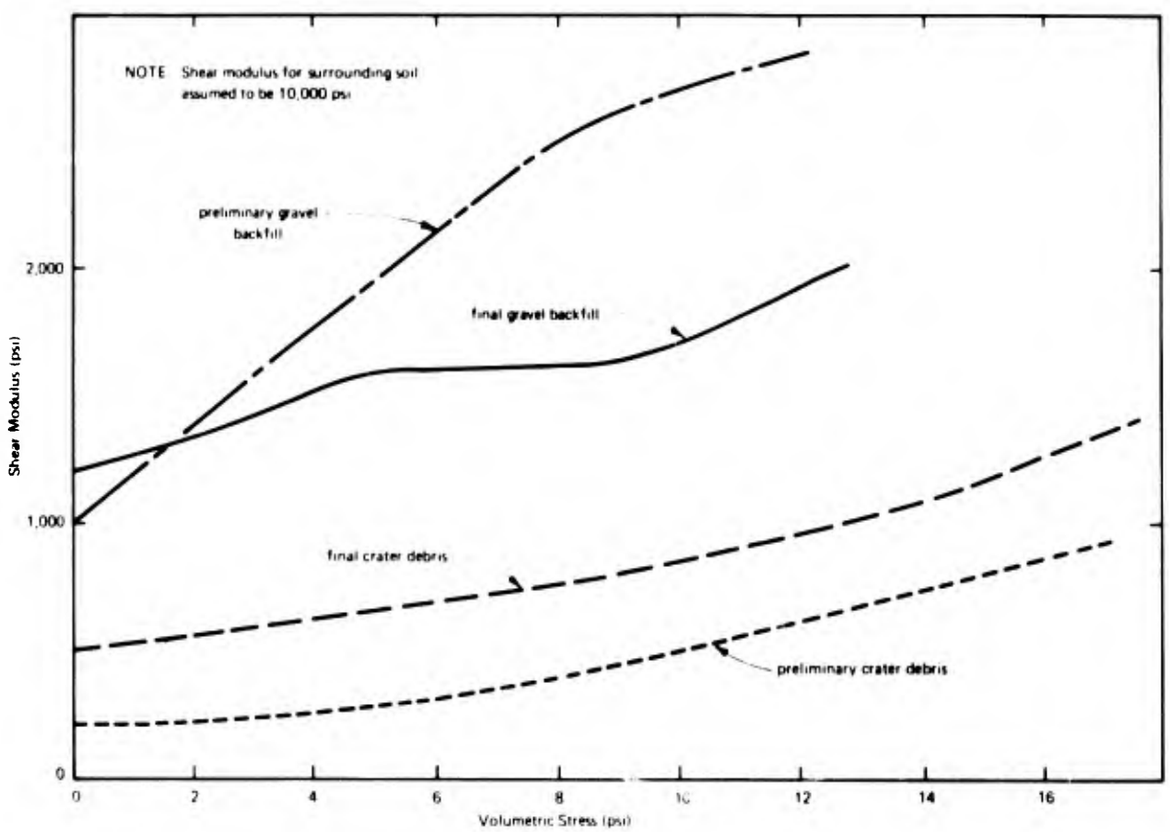

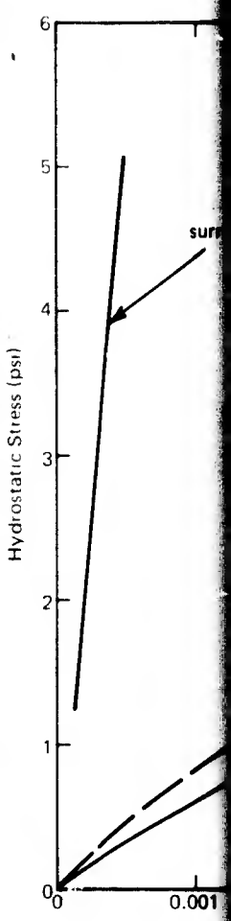

Figure 24. Material shear response for analysis of compacted model crater.

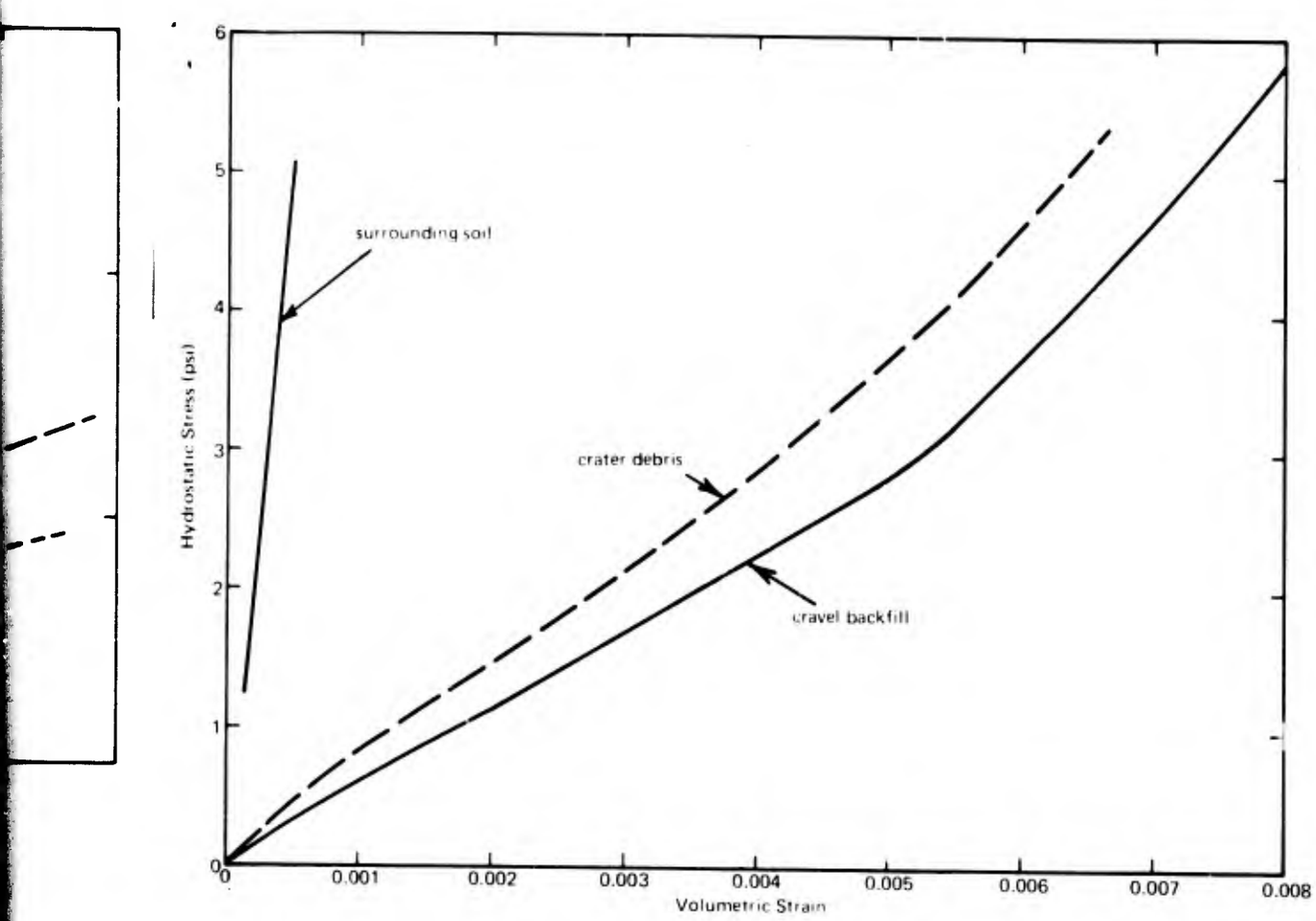

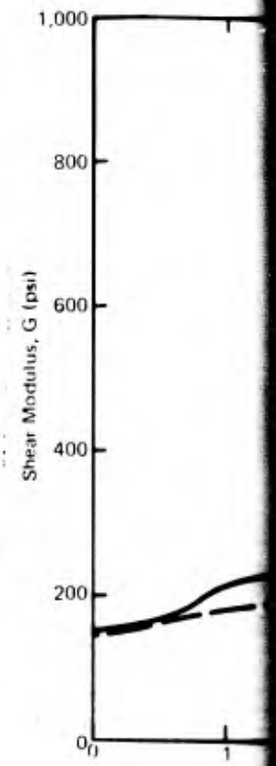

Figure 25. Material volumetric response for analysis of uncompacted model crater.

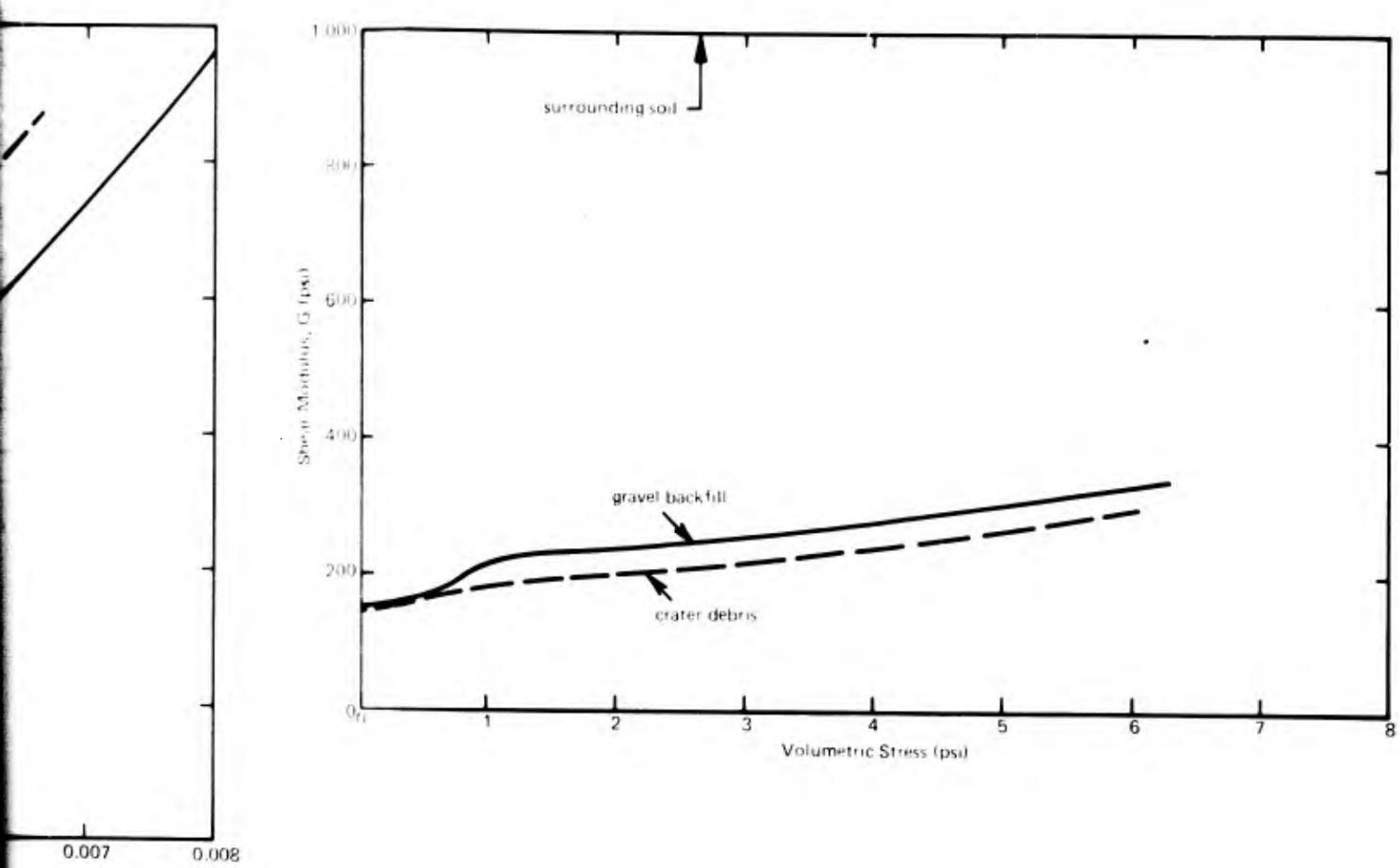

Figure 26. Material shear response for analysis of uncompacted model crater.

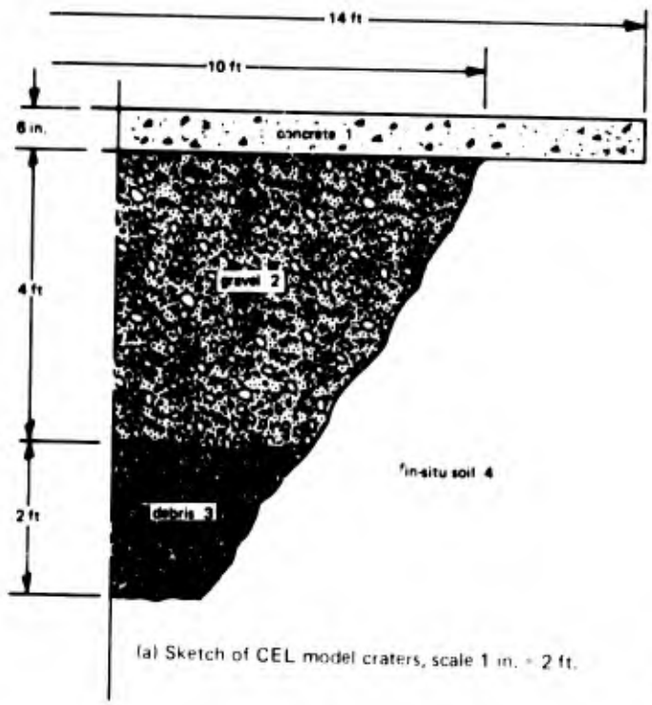

(a) Sketch of CEL model craters, scale 1 in. = 2 ft.

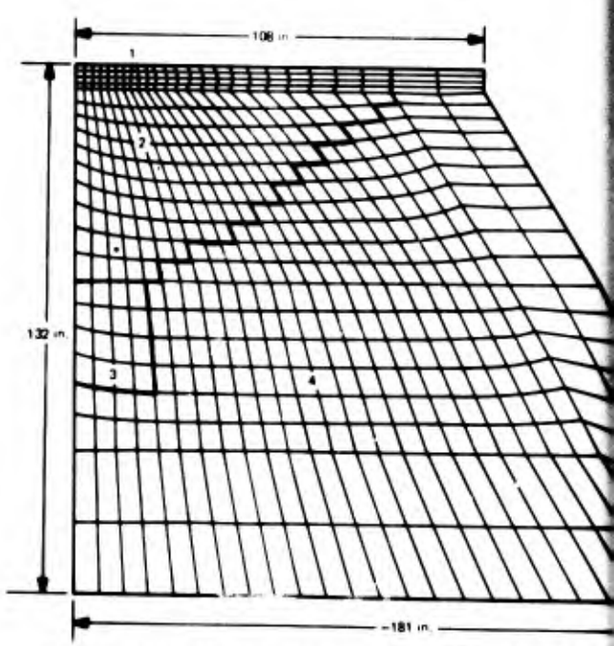

(d) Follow on to Mesh (c), where elements have been added to w

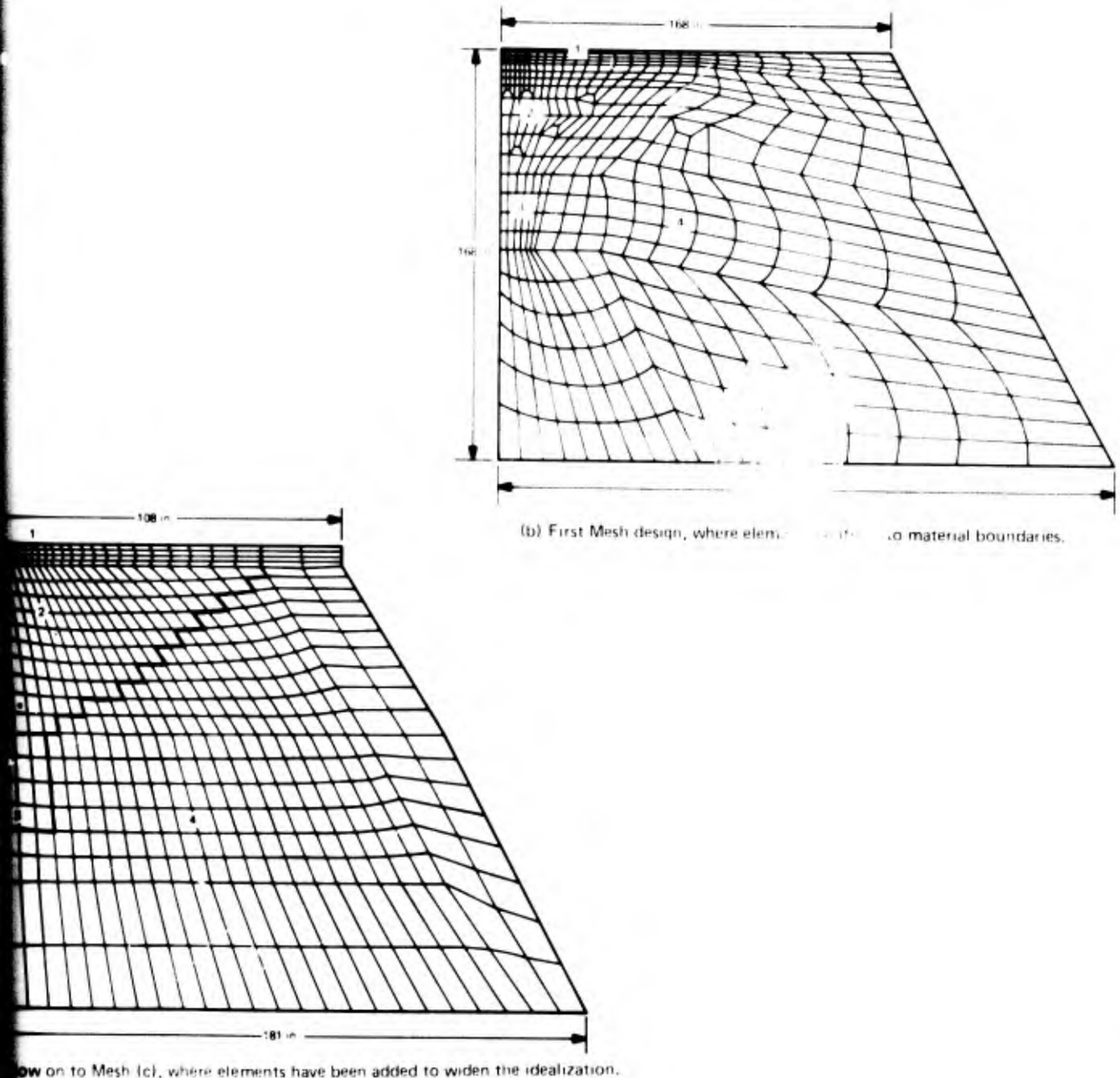

(b) First Mesh design, where elem... ...o material boundaries.

ow on to Mesh (c), where elements have been added to widen the idealization.

(e) Final Mesh configuration, **w**

Figure 27. Finite element meshes for CEL pavement tests.

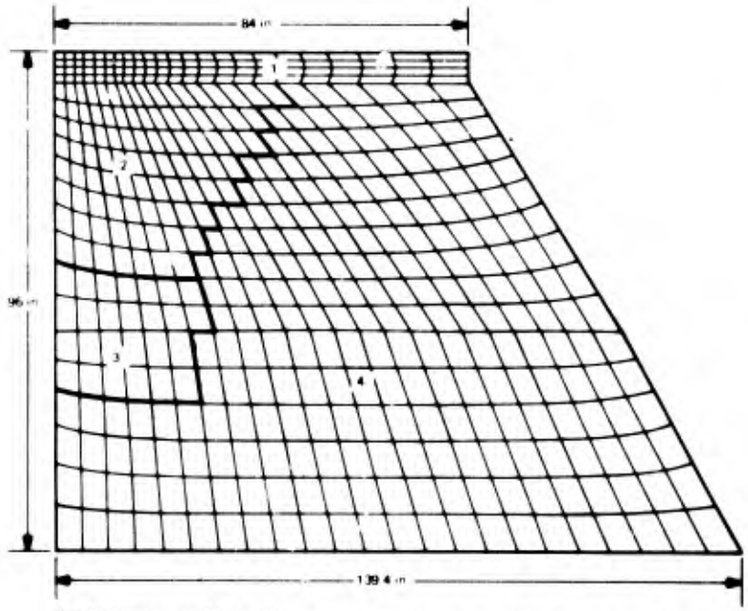

(c) Follow on to Mesh (b), where elements do not follow material boundaries.

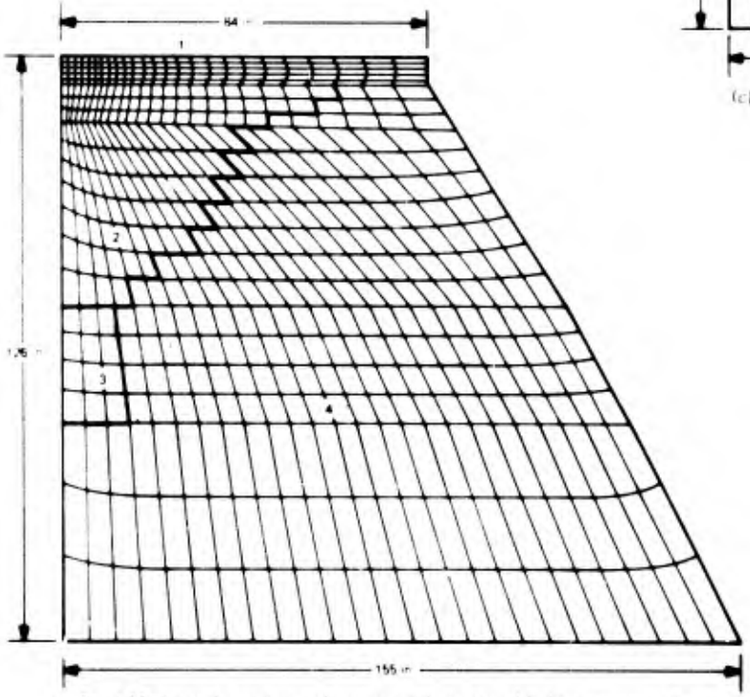

(c) Final Mesh configuration, where more elements added to pavement layer

pavement tests.